Critical Schrödinger Cat Qubit

Luca Gravina[1,2,*] Fabrizio Minganti[1,2,†] and Vincenzo Savona[1,2,‡]

[1]*Laboratory of Theoretical Physics of Nanosystems, Ecole Polytechnique Fédérale de Lausanne (EPFL), Lausanne CH-1015, Switzerland*

[2]*Center for Quantum Science and Engineering, Ecole Polytechnique Fédérale de Lausanne (EPFL), Lausanne CH-1015, Switzerland*

Encoding quantum information onto bosonic systems is a promising route to quantum error correction. In a cat code, this encoding relies on the confinement of the dynamics of the system onto the two-dimensional manifold spanned by Schrödinger cats of opposite parity. In *dissipative cat qubits*, an engineered dissipation scheme combining two-photon drive and two-photon loss has been used to autonomously stabilize this manifold, ensuring passive protection against, e.g., bit-flip errors regardless of their origin. Similarly, in *Kerr-cat qubits*, where highly performing gates can be engineered, two-photon drive and Kerr nonlinearity cooperate to confine the system to a twofold-degenerate ground-state manifold spanned by cat states of opposite parity. Dissipative, Hamiltonian, and hybrid confinement mechanisms have been investigated at resonance, i.e., for driving frequencies matching that of the cavity. Here, we propose a *critical cat code*, where both two-photon loss and Kerr nonlinearity are present and the two-photon drive is allowed to be out of resonance. The performance of this code is assessed via the spectral theory of Liouvillians in all configurations ranging from the purely dissipative to the Kerr limit. We show that large detunings and small, but non-negligible, two-photon loss rates are fundamental to achieve optimal performance. We further demonstrate that the competition between nonlinearity and detuning results in a first-order dissipative phase transition, leading to a squeezed vacuum steady state. We show that to achieve the maximal suppression of the logical bit-flip rate requires initializing the system in the metastable state emerging from the first-order transition and we detail a protocol to do so. Efficiently operating over a broad range of detuning values, the critical cat code is particularly resistant to random frequency shifts characterizing multiple-qubit operations, opening avenues for the realization of reliable protocols for scalable and concatenated bosonic qubit architectures.

I. INTRODUCTION

The development of large-scale quantum computers relies on the possibility of taming errors, i.e., the irreversible processes stemming from the interaction of the system with its surrounding environment [1–4]. Quantum error-correction schemes redundantly encode quantum information onto multilevel quantum systems, in a way that enables detection and correction of specific types of errors without affecting the stored quantum information [5–7]. The mainstream quantum error-correction paradigm consists in encoding the $|0_L\rangle$ and $|1_L\rangle$ logical states onto a two-dimensional subspace of the Hilbert space characterizing the states of several physical qubits [1,5]. Despite its promise of scalability, this type of encoding suffers from its large hardware footprint and the high connectivity between physical qubits required to execute fault-tolerant quantum computations.

An alternative paradigm to detect and correct quantum errors consists in encoding the logical states of a qubit onto an appropriately selected subspace of the Hilbert space of a harmonic oscillator [8–15]. These *bosonic quantum codes* are characterized by a reduced hardware footprint and essentially eliminate the daunting challenge of simultaneously controlling the multiple degrees of freedom of several physical qubits [16].

In these systems, information is encoded as a symmetric pattern in phase space [11]. While a translational symmetry underlies the Gottesman-Kitaev-Preskill (GKP) code [8], a rotational one characterizes the *Schrödinger-cat code*, where the logical manifold is spanned by cat states of opposite parity [9,17].

*luca.gravina@epfl.ch
†fabrizio.minganti@gmail.com
‡vincenzo.savona@epfl.ch

Schrödinger-cat qubits have been realized, in particular, on superconducting circuit platforms that are mainly prone to two noise processes: single-particle loss and dephasing [11]. These directly map onto errors on the logical qubit, namely, bit- and phase-flip errors. Confinement of the dynamics of the system to the cat manifold relies on a subtle interplay between engineered parametric processes. In recent years, two approaches have been proposed to achieve this confinement.

Dissipative confinement relies on an engineered dissipation scheme combining the two-photon drive G and the two-photon loss η [9,18–22] to generate and autonomously stabilize the code manifold. Dissipative cats are intrinsically resistant to leakage processes, ensuring an exponential suppression of the phase-flip error rate in the photon number of the cat [9,18,23,24]. Their main drawback is the limited performance of logical gates on current superconducting platforms [19,25].

Hamiltonian confinement, on the other hand, relies on the Kerr nonlinearity U to restrict the system to the doubly degenerate ground space of the Kerr parametric oscillator [26–29]. Gate performance can be improved by the application of, e.g., superadiabatic pulse designs [20], limiting the amount of leakage induced by gate operations. Nevertheless, this protocol remains susceptible to thermal and dephasing noise, which are no longer exponentially suppressed in the photon number [25]. This issue is to be ascribed to the level structure of the Kerr parametric oscillator and has been identified as the primary limitation of a *hybrid* confinement scheme, i.e., one combining sizable two-photon loss and Kerr-nonlinearity. A new confinement scheme inheriting its nonlinearity from a two-photon exchange with an external two-level system [25] has recently been proposed as a possible solution to this issue. Note that the dissipative, the Hamiltonian, and the latter proposal alike all operate in a *resonant* regime, i.e., one where the pump-to-cavity detuning is $\Delta = 0$. Only very recently, finite values of Δ have been explored, albeit restricting to the limiting case of Hamiltonian confinement, in Refs. [30–32].

Here, we adopt a novel perspective, operating the cat in a hybrid regime and in the presence of sizable detuning. We dub our encoding a *critical cat code* by virtue of the first-order dissipative phase transition (DPT) characterizing the system.

By exploring the parameter space, we prove that:

(a) Efficient quantum information encoding is not limited to $\Delta = 0$ if $U \neq 0$ but extends over a broad range of values of Δ, where the qubit can be operated (Sec. III).

(b) The critical cat *outperforms* its Hamiltonian, dissipative, and hybrid-resonant counterparts as large photon numbers and an *enhanced exponential suppression* of bit-flip errors can be achieved for carefully chosen values of Δ (Sec. III).

(c) The critical cat qubit provides a significant step forward in the hybrid operation of cat qubits, overcoming many of the limitations of the protocol detailed in Ref. [25], such as the need for additional confinement Hamiltonians other than the Kerr parametric oscillator (with annexed hardware overhead) and the lack of spontaneous stabilization (Sec. III).

(d) The code may achieve optimal performance in a regime where the code space is only metastable, while the steady state is a squeezed vacuum. In this regime, which is emerging as a consequence of the aforementioned DPT, logical errors compete with the leakage process characterizing the decay from the code space to the vacuum. Acknowledging the presence of criticality is thus fundamental for the proper characterization and initialization of detuned cat qubits, regardless of their regime of operation (Sec. IV).

(e) Parameter configurations exist for which the qubit becomes resilient against uncontrolled changes in its frequency (Sec. V), originating, for instance, from the dispersive coupling to external reservoirs or ancillary circuital elements [33,34], the latter being typically required for the realization of two-qubit entangling gates or concatenated-qubit error-correction protocols.

The paper is structured as follows. In Sec. II, we introduce the cat qubit and the dissipative and Hamiltonian processes underlying its generation and we briefly review the role of Liouvillian symmetries in bosonic quantum information encoding. In Sec. III, we analyze the effect of detuning on a hybrid cat code, demonstrating the enhanced resilience of the critical cat to bit-flip errors. In Sec. IV, we show the existence of metastable time scales and propose a protocol for the efficient initialization of detuned cats. We study the resilience to frequency-shift errors in Sec. V and discuss protocols for bias-preserving gates in Sec. VI. We draw our conclusions and discuss future perspectives in Sec. VII. Appendix A presents details on the calculations underlying the different encoding mechanisms detailed in Sec. II B. Appendix B provides an in-depth analysis of the timescales of the critical cat qubit, including the effects of thermal noise and higher-order nonlinearities.

II. GENERATION AND STABILIZATION OF SCHRÖDINGER CATS

Schrödinger-cat states are the even and odd superpositions of two coherent states of opposite phases,

$$|\mathcal{C}_\alpha^\pm\rangle = \frac{|\alpha\rangle \pm |-\alpha\rangle}{2\sqrt{1 \pm e^{-2|\alpha|^2}}}, \qquad (1)$$

where the coherent states $|\alpha\rangle$ are eigenstates of the annihilation operator $\hat{a}$, i.e., $\hat{a}|\alpha\rangle = \alpha|\alpha\rangle$ [2,35]. When

expressed in the number (Fock) basis, $\left|\mathcal{C}_\alpha^\pm\right\rangle$ contain only components with, respectively, even and odd numbers of photons. As such, they are eigenstates of the parity operator $\hat{\Pi} = \exp(i\pi\hat{a}^\dagger\hat{a})$ with eigenvalues ± 1.

Cat qubits are encoded in the two-dimensional manifold defined by cat states of opposite parity. The prevailing convention defines the logical basis as [36]

$$|0_L\rangle = \frac{1}{\sqrt{2}}\left(\left|\mathcal{C}_\alpha^+\right\rangle + \left|\mathcal{C}_\alpha^-\right\rangle\right) \approx |+\alpha\rangle + \mathcal{O}\left(e^{-2|\alpha|^2}\right)$$
$$|1_L\rangle = \frac{1}{\sqrt{2}}\left(\left|\mathcal{C}_\alpha^+\right\rangle - \left|\mathcal{C}_\alpha^-\right\rangle\right) \approx |-\alpha\rangle + \mathcal{O}\left(e^{-2|\alpha|^2}\right), \quad (2)$$

so that $|\pm_L\rangle = \left|\mathcal{C}_\alpha^\pm\right\rangle$. The generation and stabilization of Schrödinger-cat codes relies heavily on parity-preserving processes involving exclusively the pairwise exchange of photons between the system and its environment [9,17,37]. These processes are modeled by the effective Lindblad master equation [4,38–40]:

$$\partial_t\hat{\rho} = \mathcal{L}\hat{\rho} = \mathcal{L}_0\hat{\rho} + \mathcal{L}_1(\kappa_1,\kappa_\phi)\hat{\rho} \quad (3a)$$

$$\mathcal{L}_0\hat{\rho} = -i\left[\hat{H},\hat{\rho}\right] + \eta\mathcal{D}\left[\hat{a}^2\right]\hat{\rho} \quad (3b)$$

$$\hat{H} = \Delta\,\hat{a}^\dagger\hat{a} + \frac{G}{2}\left(\hat{a}^2 + \hat{a}^{\dagger 2}\right) - \frac{U}{2}\hat{a}^{\dagger 2}\hat{a}^2 \quad (3c)$$

$$\mathcal{L}_1(\kappa_1,\kappa_\phi)\hat{\rho} = \kappa_1\mathcal{D}[\hat{a}]\,\hat{\rho} + \kappa_\phi\mathcal{D}[\hat{a}^\dagger\hat{a}]\,\hat{\rho}. \quad (3d)$$

Here, $\hat{\rho} \equiv \hat{\rho}(t)$ (for brevity) is the system density matrix at time t and $\mathcal{L}$ is the Liouvillian superoperator, which we separate into two parts: $\mathcal{L}_0$ and $\mathcal{L}_1(\kappa_1,\kappa_\phi)$. The former, $\mathcal{L}_0$, confines the dynamics to the cat manifold. Its Hamiltonian $\hat{H}$ accounts for the two-photon driving-field amplitude G, the Kerr nonlinearity U, and the pump-to-cavity detuning Δ. $\mathcal{L}_0$ also accounts for two-photon losses, described by the rate η at which pairs of photons are incoherently emitted from the cavity. The latter, $\mathcal{L}_1(\kappa_1,\kappa_\phi)$, describes the unwanted effects of the environment on the code, inducing errors in the logical qubit. Here, κ_1 represents the single-photon loss rate, while κ_ϕ is the total dephasing rate.

The dissipator $\mathcal{D}\left[\hat{J}\right]$ describes the action of the jump operator $\hat{J}$ on $\hat{\rho}$ and is defined as

$$D\left[\hat{J}\right]\hat{\rho} = \hat{J}\hat{\rho}\hat{J}^\dagger - \frac{\hat{J}^\dagger\hat{J}\hat{\rho} + \hat{\rho}\hat{J}^\dagger\hat{J}}{2}. \quad (4)$$

The combined effect of $\mathcal{L}_0$ and $\mathcal{L}_1$ is usually recast in terms of a phase-flip error rate Γ_ϕ and a bit-flip error rate Γ acting on the logical qubit [9]. It is known [9,25,30,34,41–43] that the main advantage of cat qubits lies in the exponential suppression of Γ in the average photon number, with Γ_ϕ increasing only linearly. This is what drives the interest in cat states as biased-noise codes. As we show below, however, this picture is incomplete and, in most

detuned regimes of operation, at least one additional rate Γ_{leak} must be introduced, characterizing the leakage toward states outside the logical qubit manifold.

A. Symmetries

Liouvillian symmetries are distinguished into two classes: *weak* and *strong* [33,44–49]. A weak symmetry occurs when an operator $\hat{O}$ can be found that obeys

$$\mathcal{L}(\hat{O}\hat{\rho}\,\hat{O}^\dagger) = \hat{O}(\mathcal{L}\hat{\rho})\hat{O}^\dagger, \quad (5)$$

where $\mathcal{L}\hat{\rho} = -i[\hat{H},\hat{\rho}] + \sum_i \gamma_i\mathcal{D}[\hat{J}_i]\hat{\rho}$. A strong symmetry, on the other hand, requires

$$\left[\hat{O},\hat{H}\right] = \left[\hat{O},\hat{J}_i\right] = 0. \quad (6)$$

While a weak symmetry only guarantees the existence of a single steady state, a strong symmetry induces an n-dimensional steady-state manifold, where n the number of nonequivalent irreducible representations of the symmetry group [49].

The ideal Liouvillian $\mathcal{L}_0$ described in Eq. (3b) is characterized by a strong $\mathcal{Z}_2$ symmetry, as both the Hamiltonian and the jump operators commute with the parity operator $\hat{\Pi}$. The Liouvillian can thus be written in the block-diagonal form $\mathcal{L}_0 = \mathcal{L}_0^{++} \oplus \mathcal{L}_0^{+-} \oplus \mathcal{L}_0^{-+} \oplus \mathcal{L}_0^{--}$ sketched in Fig. 1(b) [50,51]. The dynamics within each block are conveniently described in terms of its eigenvalues $\lambda_j^{\mu\nu}$ and right eigenoperators $\hat{\rho}_j^{\mu\nu}$, where

$$\mathcal{L}_0^{\mu\nu}\hat{\rho}_j^{\mu\nu} = \lambda_j^{\mu\nu}\hat{\rho}_j^{\mu\nu} \quad \text{with } -\text{Re}\{\lambda_j^{\mu\nu}\} < -\text{Re}\{\lambda_{j+1}^{\mu\nu}\}. \quad (7)$$
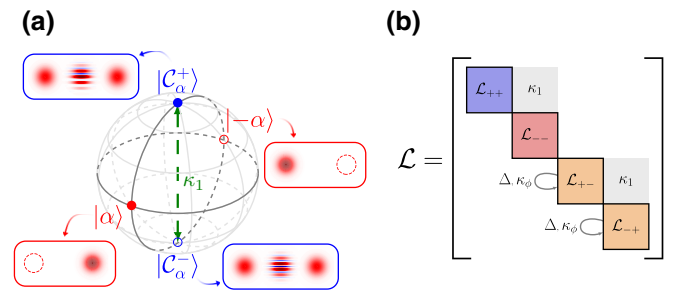

FIG. 1. (a) The even and odd cat states, represented by their Wigner functions, encode the logical states $|0_L\rangle$ and $|1_L\rangle$. Their superpositions, approximately the two coherent states $|\pm\alpha\rangle$, define the logical states $|\pm_L\rangle$. (b) The block structure of the Liouvillian arising from its strong $\mathcal{Z}_2$ symmetry. Finite values of Δ or κ_ϕ act only within the blocks $\mathcal{L}_0^{+-}$ and $\mathcal{L}_0^{-+}$, so that the four-block-diagonal structure of $\mathcal{L}_0$ is preserved. The single-photon loss κ_1, instead, connects different blocks, resulting in a two-block-diagonal structure typical of weakly $\mathcal{Z}_2$-symmetric systems.

Due to the strong symmetry, the latter are also eigenoperators of $\hat{\Pi}$ according to the relation

$$\hat{\Pi}\hat{\rho}_j^{\mu\nu} = \mu\hat{\rho}_j^{\mu\nu}, \quad \text{and} \quad \hat{\rho}_j^{\mu\nu}\hat{\Pi}^\dagger = \nu\hat{\rho}_j^{\mu\nu}. \quad (8)$$

From here on, we refer to $\hat{\rho}_0^{\mu\mu}$ as *steady states* and to $\hat{\rho}_0^{\mu\nu}$, with $\mu \neq \nu$, as *coherences* [24,50]. While the imaginary part of $\lambda_j^{\mu\nu}$ describes the oscillations within the specified sector, its negative real part sets the relaxation rate toward the steady state. Throughout the paper, we deem

$$\Lambda_j^{\mu\nu} = -\text{Re}\{\lambda_j^{\mu\nu}\}. \quad (9)$$

Complementary information on the dynamical properties of $\mathcal{L}$ can be retrieved from its left eigenoperators $\hat{\sigma}_j^{\mu\nu}$, defined as

$$\mathcal{L}_{\mu\nu}^\dagger \hat{\sigma}_j^{\mu\nu} = \left(\lambda_j^{\mu\nu}\right)^* \hat{\sigma}_j^{\mu\nu}. \quad (10)$$

They are related to $\hat{\rho}_j^{\mu\nu}$ by the biorthogonality relation

$$\text{Tr}\left[(\hat{\sigma}_k^{\mu\nu})^\dagger \hat{\rho}_j^{\mu'\nu'}\right] = \delta_{\mu,\mu'}\delta_{\nu,\nu'}\delta_{j,k} \quad (11)$$

and form a basis to express the time evolution of observables in the Heisenberg picture. The null eigenoperators $\{\hat{\sigma}_0^{\mu\nu}\}_{\mu,\nu}$ of $\mathcal{L}^\dagger$, in particular, are conserved quantities, defining the set of all observables that remain constant throughout the evolution [50].

Upon introducing single-particle loss errors with rate κ_1, the strong $\mathcal{Z}_2$ symmetry is lost, as the four-block-diagonal structure of the Liouvillian is replaced by the two-block structure $\mathcal{L} = \mathcal{L}_+ \oplus \mathcal{L}_-$ typical of the *weak $\mathcal{Z}_2$ symmetry* that persists in the system [see Fig. 1(b)]. We denote the eigenvalues of the weakly $\mathcal{Z}_2$ symmetric Liouvillian as

$$\mathcal{L}_\mu \hat{\rho}_j^\mu = \lambda_j^\mu \hat{\rho}_j^\mu \quad \text{with} \quad -\text{Re}\{\lambda_j^\mu\} < -\text{Re}\{\lambda_{j+1}^\mu\}. \quad (12)$$

Similarly, the left eigenoperators are defined as

$$\mathcal{L}_\mu^\dagger \hat{\sigma}_j^\mu = (\lambda_j^\mu)^* \hat{\sigma}_j^\mu \quad (13)$$

and in analogy to Eq. (9), we define the rates

$$\Lambda_j^\mu = -\text{Re}\{\lambda_j^\mu\}. \quad (14)$$

Within this picture, an arbitrary state *will decay toward the unique steady state of the system*.

B. Quantum information encoding

An open quantum system can encode quantum information and perform quantum computation (details in Appendix A) if, at time $t = 0$, the following relation holds:

$$\hat{\rho}(0) \equiv \hat{Q}(0) \otimes \hat{M}(0). \quad (15)$$

The matrix $\hat{\rho}(0)$ is that of a bipartite system, where $\hat{Q}(0)$ is the state encoding quantum information, while $\hat{M}(0)$ is

a mixed state. Hamiltonian and dissipative processes will make the system evolve into

$$\hat{\rho}(t) = \beta(t)\hat{Q}(t) \otimes \hat{M}(t) + [1 - \beta(t)]\hat{\rho}_{\text{leak}}(t), \quad (16)$$

where $\hat{\rho}_{\text{leak}}$ represents the leakage outside the code space, $\beta(t)$ is determined by the Liouvillian dynamics, and we neglect possible coherences between the code and the leakage space. If $\beta(t) = 1$, the Liouvillian dynamics will not induce leakage. In this case, the evolution $Q(t)$ represents that of a logical qubit in the presence of logical bit- (Γ) and phase-flip (Γ_ϕ) errors. The special case of $\hat{Q}(0) = \hat{Q}(t)$, i.e.,

$$\hat{\rho}(t) = \hat{Q}(0) \otimes \hat{M}(t), \quad (17)$$

corresponds to $\Gamma = \Gamma_\phi = 0$. This is a *noiseless subsystem* [1,13,23,51–54] and it can only emerge in the system under investigation if $\kappa_1 = \kappa_\phi = \Delta = 0$ [9,33]. Indeed, only when a zero Liouvillian eigenvalue exists within each symmetry sector, i.e., $\Lambda_0^{\mu\nu} = 0 \ \forall \mu, \nu \in \{\pm\}$, can quantum information be stored indefinitely, as this guarantees infinitely long-lived steady states and coherences. If, instead, $\kappa_1, \kappa_\phi, \Delta \neq 0$, and $\beta(t) = 1$, the system will evolve toward its unique steady state as

$$\hat{\rho}(t) = \hat{Q}(t) \otimes \hat{M}(t). \quad (18)$$

For the logical qubit, this corresponds to finite values of Γ and Γ_ϕ and will result in the irreversible evolution of the qubit toward a steady state at the center of the Bloch sphere. We refer to this case as the *steady-state encoding*.

If, instead, $\beta(t) < 1$, the system will leak out of the code space. This case implies the existence of at least one additional time scale $1/\Gamma_{\text{leak}}$, governing the variation of $\beta(t)$. A limiting case in this scenario, which we call a *metastable encoding*, is

$$\hat{\rho}(t) = \beta(t)\hat{Q}(t) \otimes \hat{M}(t) + [1 - \beta(t)]\hat{\rho}_{\text{ss}},$$
$$\beta(t) = 1 - e^{-\Gamma_{\text{leak}}t}. \quad (19)$$

As we show below, an optimal biased-noise metastable encoding—wherein quantum information can be efficiently stored—requires Γ and Γ_{leak} to be very small with respect to the typical rate of gate operations.

III. ENHANCED SUPPRESSION OF BIT-FLIP ERRORS

Dissipative, Hamiltonian, and hybrid stabilization alike have mainly been investigated at $\Delta = 0$, where, in the absence of errors, Eq. (15) is exactly met. In this section, we unveil Δ as a new control parameter, demonstrating its potential to significantly enhance the performance of cat codes.

As we are interested in the cat code as a biased-noise encoding, we focus in this section on finding the optimal parameter configuration minimizing the bit-flip error rate Γ in the presence of both photon-loss and dephasing errors. For consistency with the existing literature [25,29–31,34], we take $0 < G < 8$ and consider throughout this section two noise configurations: one dominated by photon-loss ($\kappa_1 = 10^{-3} \gg \kappa_\phi = 10^{-5}$) and the other by dephasing ($\kappa_1 = 10^{-5} \ll \kappa_\phi = 10^{-3}$). We defer a thorough analysis of the interplay between Γ and Γ_{leak} and of the different encoding emerging at finite detuning to Sec. IV and Appendix A.

A. Liouvillian analysis of critical cat

In this section, we analyze the spectral properties of $\mathcal{L} = \mathcal{L}_0 + \mathcal{L}_1$ [Eq. (3)] to gain insight into the interplay between Δ, U and/or η in relation to Γ. We relate these parameters by setting

$$\eta = W\cos(\theta), \quad U = W\sin(\theta), \quad \eta^2 + U^2 = W^2, \quad (20)$$

where W represents the natural unit of the system. In what follows, all energies and times are reported in units of W and W^{-1}, respectively. By varying θ between 0 and $\pi/2$, we are able to continuously explore the hybrid region between the dissipative and Hamiltonian (Kerr) limits. We do so in Fig. 2 where, for a fixed value of G, we explore the phase diagram of Λ_0^- in Δ and $U/\eta = \tan(\theta)$ for both noise configurations. Within this Liouvillian picture, $\Gamma \equiv \Lambda_0^-$ represents the slowest time scale involved in the decay of the field quadratures. For instance, it describes the rate at which $|\alpha\rangle \rightarrow |-\alpha\rangle$ whenever $\Delta = 0$ [24,31].

While in the dissipative limit ($U/\eta < 1$) the detuning configuration minimizing Γ is the resonant one ($\Delta_{\text{opt}} = 0$), for sizable Kerr nonlinearities ($U/\eta > 1$) $\Delta_{\text{opt}} > 0$. Indeed, in this regime, the introduction of a nonvanishing detuning significantly suppresses the value of Γ not only with respect to the physical error rates but to all resonant configurations as well. This result is at the heart of the *critical cat code*, as it highlights the key role of detuning in suppressing bit-flip errors, with its effectiveness being linked to the presence of a nonzero Kerr nonlinearity (see Fig. 2).

In this direction, comparison of Figs. 2(a) and 2(b) shows that in a configuration dominated by dephasing, the optimal Γ is found deep in the hybrid regime ($U/\eta \approx 10^2$), while in a configuration dominated by photon loss, it is achieved closer to the Kerr limit ($U/\eta \gtrsim 10^5$). This is further supported by Fig. 3, which displays $\Gamma(\Delta_{\text{opt}})$ as a function of κ_1 and U/η, for different values of κ_ϕ. The data reveal that the region with optimal protection from errors progressively shifts from the hybrid phase to the Kerr limit as κ_ϕ is decreased. This trend can be observed for all values of κ_1, although it becomes more pronounced for $\kappa_1 \gg \kappa_\phi$.
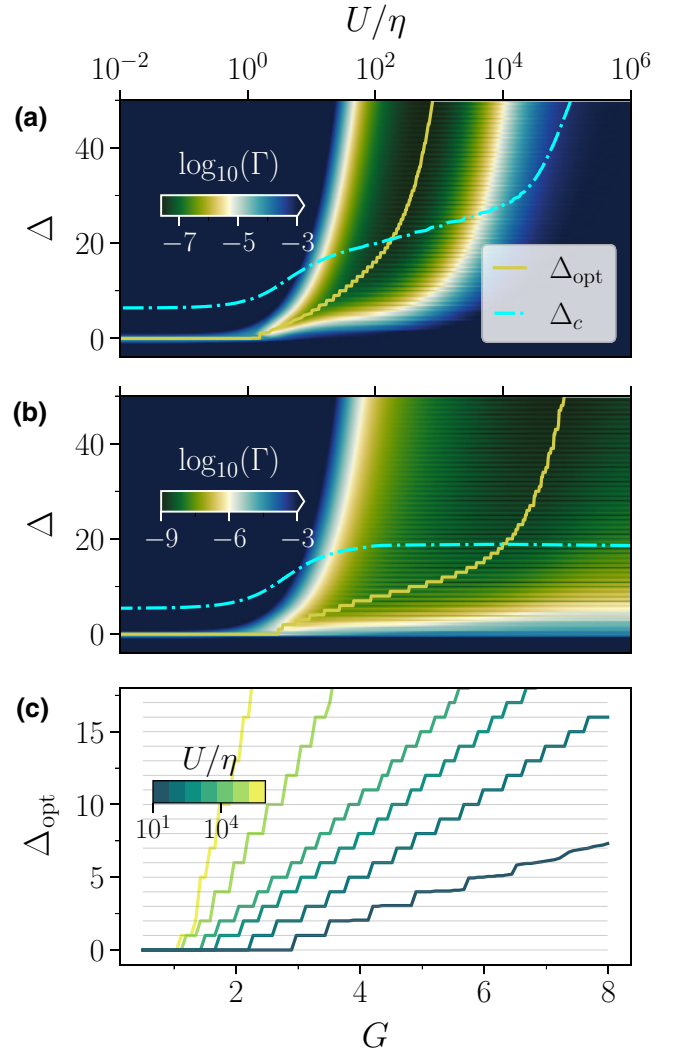

FIG. 2. (a),(b) The bit-flip error rate Γ as a function of the detuning Δ and the ratio $U/\eta = \tan(\theta)$ defined in Eq. (20). The dissipative limit corresponds to $\theta = 0$ ($U = 0$, $\eta = 1$). The opposite limit, i.e., the Kerr (or Hamiltonian) limit, is reached for $\theta = \pi/2$ ($U = 1$, $\eta = 0$). The optimal detuning values $\Delta_{\text{opt}}(G = 5, \theta)$ are shown as continuous yellow lines. The dot-dashed line denotes the critical threshold Δ_c separating the phase with large steady-state photon number from the vacuum one (see Sec. IV). We set the two-photon driving-field amplitude $G = 5$ and (a) $\kappa_1 = 10^{-5} \ll \kappa_\phi = 10^{-3}$ and (b) $\kappa_1 = 10^{-3} \gg \kappa_\phi = 10^{-5}$. (c) $\Delta_{\text{opt}}(G, \theta)$ as a function of G for different values of θ and $\kappa_1 = 10^{-3} \gg \kappa_\phi = 10^{-5}$.

Note that although Δ_{opt} is rapidly increasing in U/η (yellow solid lines), for both noise configurations we find large regions in the parameter space where Γ does not significantly depart from its optimal value. While in the photon-loss-dominated case, this region extends from a hybrid to a purely Kerr regime [Fig. 2(b)], in the dephasing-dominated one, it always requires nonvanishing η [Fig. 2(a)]. Overall, this introduces a trade-off between the choice of θ
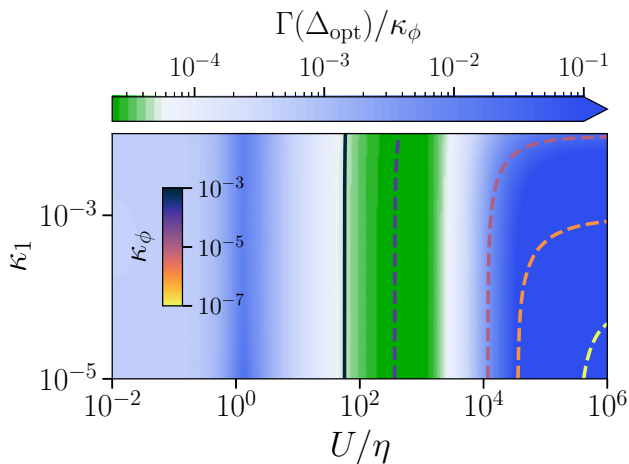
FIG. 3. The optimal bit-flip error rate $\Gamma(\Delta_{\mathrm{opt}})$ as a function of the single-photon loss rate κ_1 and of the ratio U/η for $\kappa_\phi = 10^{-3}$. The value of $\Gamma(\Delta_{\mathrm{opt}})$ is normalized to κ_ϕ to ensure consistency in the limiting values of the displayed quantity for all choices of κ_ϕ. The solid line highlights the lowest-(U/η) isoline $\Gamma(\Delta_{\mathrm{opt}})/\kappa_\phi = 5 \times 10^{-5}$. The dashed curves display the same quantity for $\kappa_\phi = 10^{-4}$, 10^{-5}, 10^{-6}, and 10^{-7}. The optimal configuration is clearly seen to shift toward the Kerr limit for increasing values of κ_ϕ.

and the attainable values of Δ, which is an experimentally finite resource. Indeed, for very large detuning, the approximations leading from a microscopic description to the effective model in Eq. (3) break down. For this reason, we restrict our considerations to $\Delta \leq \Delta_{\mathrm{max}} = 50$, consistently with the most recent experimental efforts in this direction [32]. In Fig. 2(c), we characterize the behavior of Δ_{opt} as a function of G for various values of U/η. The increase of Δ_{opt} follows a staircase pattern, taking on integer multiples of U for which additional degeneracies in the spectrum of the Kerr parametric oscillator have been found [30–32]. This staircase pattern is particularly pronounced in the hybrid regime, becoming steeper in the Kerr limit, consistently with the aforementioned divergence of Δ_{opt} in U/η.

B. Scaling of bit-flip error rates

Having shown the advantage of the hybrid critical encoding for $G = 5$, we set out to demonstrate the enhanced exponential suppression of Γ with the average photon number $\langle \hat{a}^\dagger \hat{a} \rangle \propto G$. In Fig. 4, we assess the scaling of Γ as a function of G for several values of θ and Δ. As baselines for the assessment of the critical cat, we consider the resonant dissipative (blue) and Hamiltonian (yellow) limits. As expected [25], the dissipative confinement shows an exponential suppression of Γ, significantly outperforming its Kerr counterpart. We verify that if we set $\Delta = 0$ and optimize Γ over θ alone, the optimal point coincides with the dissipative limit ($\theta_{\mathrm{opt}}|_{\Delta=0}$
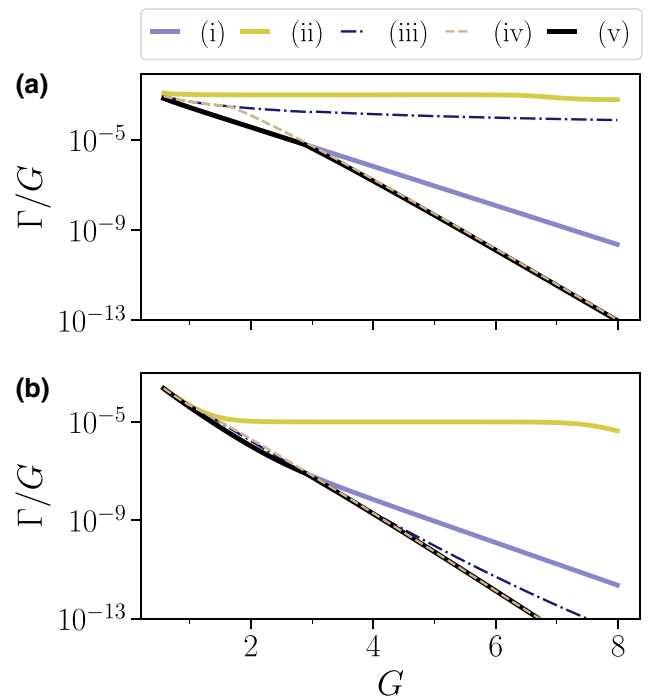

FIG. 4. The bit-flip error rate Γ as a function of the driving-field amplitude G for different values of Δ and θ, for (a) $\kappa_1 = 10^{-5} \ll \kappa_\phi = 10^{-3}$ and (b) $\kappa_1 = 10^{-3} \gg \kappa_\phi = 10^{-5}$. In both panels, we display results for (i) the Kerr limit $U/\eta = 10^6$, (ii) the dissipative limit $U/\eta = 0$, (iii) the optimal configuration obtained by optimizing both θ and Δ, and (iv) the result obtained by setting $U/\eta = 10^6$ and optimizing over Δ. The curve denoted as (v) is obtained by setting $U/\eta = 10^2$ in (a) and $U/\eta = 10^5$ in (b).

$= 0$). We thus move to consider the effect of Δ. By setting $\theta = 0$ and optimizing over Δ alone, we find that $\Delta_{\mathrm{opt}}|_{\theta=0} = 0$. In the dissipative limit, therefore, there is no advantage in introducing a nonvanishing detuning. In the Kerr limit ($U/\eta = 10^6$) instead, optimizing Δ introduces only a marginal advantage in the dephasing-dominated configuration [Fig. 4(a)] in the configuration dominated by photon-loss [Fig. 4(b)]. Finally, we consider the combined optimization of θ and Δ. We verify that the critical cat code significantly outperforms its resonant counterparts and confirm that in the dephasing-dominated case, for all $G > 3$, the optimum is found deep in the hybrid regime ($U/\eta \approx 10^2$), while in the photon-loss-dominated one, it approaches the Kerr limit ($U/\eta \gtrsim 10^5$).

We now set out to demonstrate the enhanced scaling of Γ as a function of the photon number in the critical cat. We find that in the driving range $4 < G < 12$, all curves display the functional dependence $\Gamma/G \simeq \Gamma_0 \exp\{-\zeta G\}$, which we use to extract the scaling coefficient $\zeta(\theta, \kappa_1, \kappa_\phi)$. The results are shown in Fig. 5 as a function of the ratio
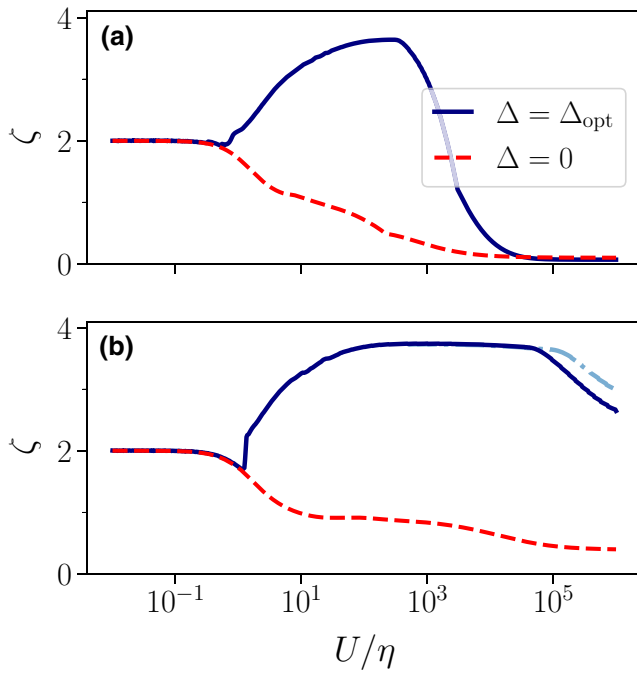
FIG. 5.   The exponential rate ζ computed as a function of U/η for $\Delta = 0$ (dashed) and $\Delta = \Delta_{\text{opt}}$ (solid): (a) $\kappa_1 = 10^{-5} \ll \kappa_\phi = 10^{-3}$; (b) $\kappa_1 = 10^{-3} \gg \kappa_\phi = 10^{-5}$. The dot-dashed curve in (b) shows $\zeta(\Delta_{\text{opt}})$ for $\Delta_{\text{max}} = 90$.

U/η. As also predicted in Ref. [25], for $\Delta = 0$, the system progressively loses its protection against dephasing-induced bit-flip errors as it transitions from the dissipative to the Hamiltonian limit. On the contrary, operating the critical cat at $\Delta = \Delta_{\text{opt}}(G)$ endows the system with an additional resilience to errors, so that the bit-flip error rate is not only exponentially suppressed in the photon number but it does so with an enhanced scaling coefficient compared to its optimal resonant value $\zeta = 2$ achieved in the purely dissipative regime. To clarify the relevance of the bound Δ_{max}, Fig. 5(b) also shows the rate ζ obtained by setting $\Delta_{\text{max}} = 90$. This larger bound results in a marginal increase of the favorable range of values of U/η, as also expected from the analysis of $\Delta_{\text{opt}}(\theta)$ in Fig. 2. We finally draw attention to the fact that in a realistic framework, where detuning is a limited resource, the presence of a small two-photon loss is essential to achieve optimal scaling and operating with a pure Kerr confinement can result in severe underperformance of the cat.

Overall, we demonstrate the existence of regions in parameter space granting enhanced protection from bit-flip errors. Our findings also resolve the issues tied to the hybrid operation of Kerr-cat qubits outlined in Ref. [25] and discussed in Sec. I. Finally, we remark that in this section we treat U/η as a free parameter, although in general U and η represent distinct and limited resources. Nonetheless, we show that the optimal configuration is one

where $\eta \sim \kappa_1$, $\kappa_\phi \ll U$. It is thus possible to achieve these values starting from a Kerr-qubit architecture through reservoir engineering techniques, as demonstrated in previous works [18,29].

IV. METASTABLE ENCODING AND THE CRITICAL CAT

The analysis until now has focused on the minimization of Γ alone. We now consider the interplay between Γ and Γ_{leak} and the various possible encodings.

A fundamental property of the two-photon driven-dissipative Kerr resonator is the occurrence of a first-order DPT at a critical detuning Δ_c, resulting in a discontinuous change in the steady state of the system [55–57]. Here, we show that this phase transition has profound consequences on the encoding and determines the way in which the qubit must be prepared and controlled to achieve optimal performance. The DPT arising for a specific choice of parameters is shown in Fig. 6(a). Here, the photon number of the system is seen to change abruptly as Δ is increased beyond Δ_c [58]. Indeed, while for $\Delta < \Delta_c$ the steady state of the system defines a highly populated phase (catlike), for $\Delta > \Delta_c$, the steady state approximates the squeezed vacuum state.

Figures 2(a) and 2(b) detail the dependence of Δ_c on θ, marking the boundary between the two phases. This figure shows that Δ_{opt} minimizing Γ crosses Δ_c as the ratio U/η is increased. A fundamental question is therefore which kind of encoding among those introduced above holds in each phase. Another main result of our work consists in showing that the two phases identified above express different encodings, with the metastable encoding in Eq. (19) characterizing all largely detuned configurations. This is a pivotal point, as now Γ_{leak} also contributes to the performance of the code. This effect has been overlooked when modeling the cat code within a purely Hamiltonian formalism, oblivious to the DPT. We also show that the critical behavior affects the initialization of the code in either phase and we provide an initialization protocol that prevents the system from being pinned to the squeezed vacuum. All in all, accounting for the critical behavior of the cat code at finite values of Δ, η, κ_1, and κ_ϕ is key to determining an optimal encoding protocol.

The analysis that follows assumes $G = 5$, $U/\eta = 10^5$, and $\kappa_1 = 10^{-3} \gg 10^{-5} = \kappa_\phi$.

A. Criticality and metastability

Two types of critical phenomena can occur in open quantum systems: first- and second-order phase transitions [55–57,59–70]. The former (latter) corresponds to a discontinuous (continuous but not differentiable) change in the properties of the system, the finite-size precursor of which is shown in Fig. 6(a), which displays the steady-state photon number as a function of Δ. Upon crossing the
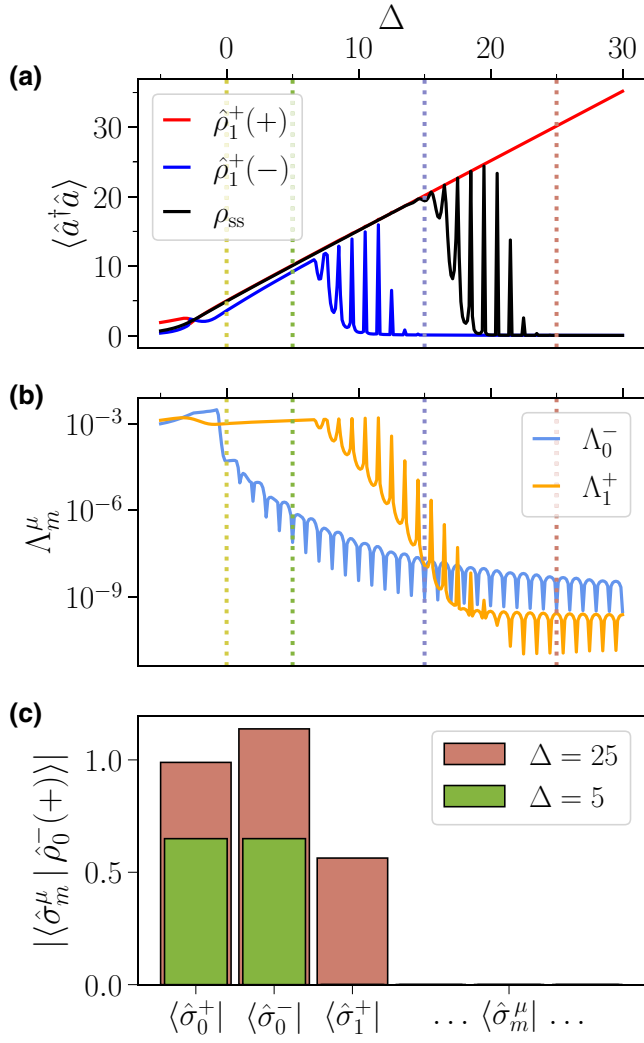
FIG. 6. (a) The average photon number of the steady and metastable states as defined in the text. The jump discontinuity in the photon number signals the presence of a first-order DPT at $\Delta_c \sim 15$ [58]. (b) The Liouvillian gaps Λ_1^+ and Λ_0^- as defined in Eq. (12). The vertical dotted lines denote the values of Δ selected for further investigation in Fig. 9. (c) Expansion of the state $\hat{\rho}_0^-(+) \equiv |1_L\rangle\langle 1_L|$ [cfr Eq. (22)] in the left eigenstates of $\mathcal{L}$. The expansion coefficients are $c_m = \langle \sigma_m^\mu | \hat{\rho}_0^-(+) \rangle$. Each component in the expansion evolves with one specific time scale. For $\Delta < \Delta_c$, only two components are nonvanishing: the steady state and that corresponding to bit flips. For $\Delta > \Delta_c$, a single additional component corresponding to the leakage with rate $\Gamma_{\text{leak}} = \Lambda_1^+$ emerges and the dynamics are that of Eq. (19). We consider $G = 5$, $U/\eta = 10^5$, and $\kappa_1 = 10^{-3} \gg 10^{-5} = \kappa_\phi$.

critical value Δ_c, an abrupt transition from a highly populated to a squeezed vacuum phase (from here onward, *vacuum* for brevity) occurs. We verify that Δ_c is only marginally affected by the values of (κ_1, κ_ϕ). The hallmark of a first-order DPT is the closure of the Liouvillian gap Λ_1^+ [64,71,72], the finite-size precursor of which is shown

in Fig. 6(b). This closure entails metastability and is associated with a hysteretic behavior of the system, which, despite the uniqueness of the steady state, can persist in other states for very long times.

In the cat code, a biased response to noise requires the existence of two opposite points on the logical Bloch sphere, between which noise-induced transitions are exponentially suppressed. Without loss of generality, we can identify these two points as the logical states $|0_L\rangle$ and $|1_L\rangle$. These states are defined through the following procedure [71,73]. We start from the eigenoperator $\hat{\rho}_0^-$, which in its diagonal form reads

$$\hat{\rho}_0^- = \sum_i p_i |\psi_i\rangle\langle\psi_i|. \tag{21}$$

Because $\hat{\rho}_0^-$ is Hermitian, all the p_i are real and $\langle\psi_i|\psi_j\rangle = \delta_{ij}$. Since $\text{Tr}[\hat{\rho}_0^-] = 0$, some p_i will be positive while others are negative and we can order them in such a way as to have $p_i > 0$ ($p_i < 0$) for $i \leq \bar{i}$ ($i > \bar{i}$). In this way, $\hat{\rho}_0^- = \hat{\rho}_0^-(+) - \hat{\rho}_0^-(-)$ with

$$\hat{\rho}_0^-(+) = \sum_{i \leq \bar{i}} p_i |\psi_i\rangle\langle\psi_i|, \quad \hat{\rho}_0^-(-) = -\sum_{i > \bar{i}} p_i |\psi_i\rangle\langle\psi_i|. \tag{22}$$

The probabilities p_i are normalized to ensure that $\text{Tr}[\hat{\rho}_0^-(\pm)] = 1$. The logical states of the code are then defined as

$$|0_L\rangle\langle 0_L| = \hat{\rho}_0^-(+), \quad |1_L\rangle\langle 1_L| = \hat{\rho}_0^-(-). \tag{23}$$

This definition ensures that the bit-flip rate $\Gamma = \Lambda_0^-$ coincides with the slowest decay rate of the off-diagonal Liouvillian sector. Additionally, for all cases considered below, the logical qubit will undergo decoherence at a rate Γ_ϕ—the noise mechanism not suppressed by the cat encoding.

We identify three regimes:

(1) $\Delta = 0$. Here, $\hat{\rho}_0^- \propto |\alpha\rangle\langle\alpha| - |-\alpha\rangle\langle-\alpha|$; thus $|0_L\rangle = |\alpha\rangle$ and $|1_L\rangle = |-\alpha\rangle$. The very same states also define $\hat{\rho}_{ss} \simeq (|\alpha\rangle\langle\alpha| + |-\alpha\rangle\langle-\alpha|)/2$ [74], which is located at the center at the Bloch sphere (see illustration in Fig. 7). This is the steady-state encoding defined in Eq. (18) for which the states $|0_L\rangle$ and $|1_L\rangle$ are *only* exchanged at a rate Γ.

(2) $0 < \Delta < \Delta_c$. While $\hat{\rho}_0^-$ cannot be expressed as a simple mixture of two coherent states, as in the case when $\Delta = 0$, a steady-state encoding still holds (as illustrated in Fig. 7), since $\hat{\rho}_{ss} \simeq |0_L\rangle\langle 0_L| + |1_L\rangle\langle 1_L|$. The spectral decomposition in Fig. 6(c) demonstrates that also in this regime, $|0_L\rangle$ and $|1_L\rangle$ *only* flip at a unique rate Γ. As Δ approaches Δ_c, the vacuum

state becomes progressively more stable, as shown by the decrease of Λ_1^+ in Fig. 6(b). This increased stability makes the initialization of the code more challenging, as the system tends to remain pinned to the long-lived vacuum state.

(3) $\Delta > \Delta_c$. In this regime, $\hat{\rho}_{\mathrm{ss}} \simeq |n=0\rangle\langle n=0| \neq |0_L\rangle\langle 0_L| + |1_L\rangle\langle 1_L|$. This is a metastable encoding according to Eq. (19). Indeed, all processes within the code space can still be described in terms of the logical error rates Γ and Γ_ϕ. All states initialized on the logical Bloch sphere will, however, irreversibly decay toward $\hat{\rho}_{\mathrm{ss}}$, which now lies outside of the code space. This process occurs at a rate $\Lambda_1^+ = \Gamma_{\mathrm{leak}}$. The center of the Bloch sphere, which previously coincided with $\hat{\rho}_{\mathrm{ss}}$, is now $\hat{\rho}_1^+(+)$ and is obtained by the spectral decomposition

$$\hat{\rho}_1^+ = \hat{\rho}_1^+(+) - \hat{\rho}_1^+(-), \qquad (24)$$

defined in analogy to Eqs. (21) and (22). Indeed, while $\hat{\rho}_1^+(-)$ closely resembles the vacuum-like steady state, $\hat{\rho}_1^+(+) \propto |0_L\rangle\langle 0_L| + |1_L\rangle\langle 1_L|$ (see Fig. 14). In this regime, the quality of the encoding will thus depend not only on the magnitude of Γ and Γ_ϕ but on that of Γ_{leak} as well. Our simulations suggest, for $\Delta_{\mathrm{opt}} > \Delta_c$, the rates Γ and Γ_{leak} may have comparable magnitudes, as can be inferred from the data in Fig. 6(b).

We remark that both Λ_0^- and Λ_1^+ display oscillations with sharp minima. While the minima of Λ_0^- occur at $\Delta \simeq Um$ with $m \in \mathbb{N}$, those of Λ_1^+ occur at $\Delta = (m + 1/2)U$, where Λ_0^- has maxima. While in the regime where
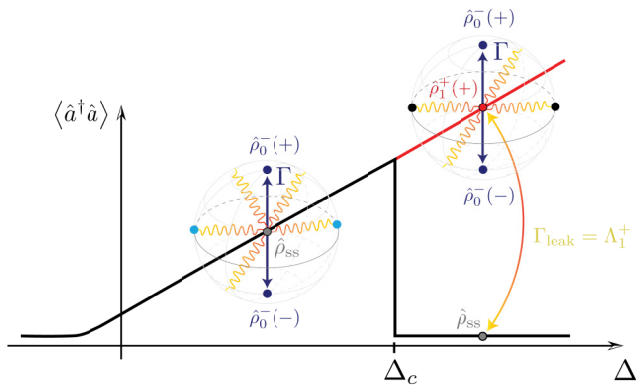

FIG. 7. An illustration of the optimal encoding on the two sides of the phase boundary. For $\Delta < \Delta_c$, the steady-state manifold coincides with the encoding manifold and the logical code space is characterized by a single phase-flip error rate Γ. For $\Delta > \Delta_c$, the steady state is a squeezed vacuum and is distinct from the optimal encoding manifold characterized by a finite average photon number. In this case, a second time scale emerges, which is characterized by the rate Λ_1^+ at which the logical states decay into the vacuum.
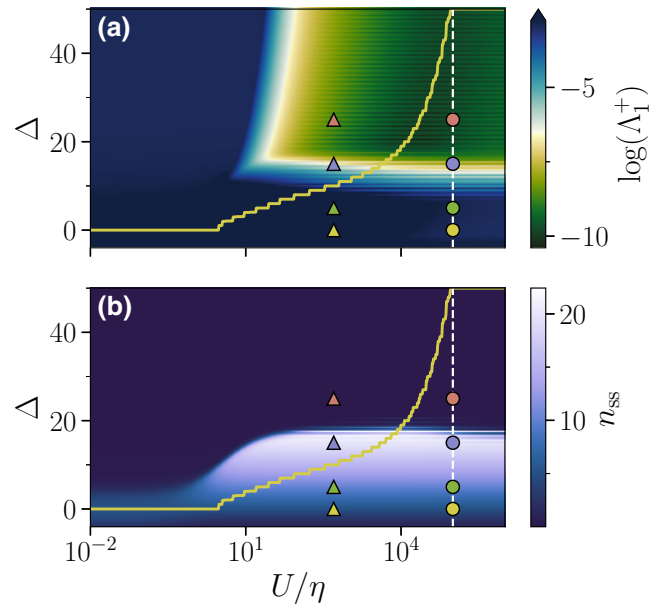

FIG. 8. The phase diagrams of (a) the diagonal Liouvillian gap Λ_1^+ and (b) the steady-state photon number as a function of the detuning Δ and the ratio U/η. The yellow line denotes the optimal detuning Δ_{opt} that minimizes the bit-flip error rate Γ. The circles and triangles indicate the specific cases selected for the discussion of the state-preparation protocol in Sec. IV B and shown in Fig. 9.

a steady-state encoding holds, Λ_1^+ does not affect the performance of the code, in the one characterized by a metastable encoding, $\Lambda_1^+ = \Gamma_{\mathrm{leak}}$ defines a source of uncorrectable errors. Because for the detuning values minimizing Λ_0^-, Λ_0^- and Λ_1^+ become comparable, a trade-off between these two error processes emerges when deciding at which detuning to operate the code. The conclusions drawn here hold in both noise configurations and throughout the range $10^2 \leq U/\eta \leq 10^5$. Additional results in this direction are presented in Appendix B. From these data, we note that these oscillatory features become less pronounced the larger the η that we take.

In Fig. 8, we finally display the Liouvillian gap Λ_1^+ and the steady-state average photon number as a function of Δ and U/η. As U/η increases, the optimal detuning Δ_{opt} crosses the phase boundary, identifying large regions in the parameter space where the optimal encoding is the metastable one. In all parameters considered, the sudden drop in the photon number is accompanied by a reduction in Λ_1^+, minimal around Δ_{opt}. Comparing Figs. 8(a) and 2(b), we conclude that a minimal leakage error Γ_{leak} accompanies the minimal Γ. These data support the above analysis, demonstrating that the presence of a metastable encoding is an emergent feature of the cat code at finite detuning and highlighting the key role of criticality in determining the optimal encoding.

B. State-preparation protocol

The scenario described above indicates that the code space is stable and the vacuum metastable whenever $\Delta < \Delta_c$, while the converse is true for $\Delta > \Delta_c$. Assuming a preparation protocol where, starting from the vacuum, the two-photon driving field G is ramped up, two issues may arise. For $\Delta < \Delta_c$, the system will remain stuck in the vacuum for a time $1/\Lambda_0^-$ before reaching the stable code space. For $\Delta > \Delta_c$, the system will never leave the stable vacuum and thus will never reach the metastable code space. We simulate this simple ramp-up protocol for the exemplary noise configuration with $\kappa_1 = 10^{-3} \gg 10^{-5} = \kappa_\phi$ and display the results in Fig. 9, confirming the above predictions.

We propose a solution for this initialization problem taking advantage of criticality. While the system undergoes a first-order DPT for $\Delta > 0$, a second-order DPT takes place at $\Delta < 0$ [55,70,71]. As shown in Ref. [75–77], around a second-order DPT, the system is highly responsive and does not experience critical slowing down if properly initialized. We take advantage of this property in a protocol where Δ is ramped up rather than G. We start from $\Delta_0 \equiv \Delta(t = 0) < G$, with the system in the vacuum state and G fixed at its target value. We then increase $\Delta(t)$ according to a schedule

$$\Delta(t) = \Delta_0 + f(t, \tau)(\Delta - \Delta_0), \qquad (25)$$

where $f(t, \tau)$ a smooth function increasing from $f(0, \tau) = 0$ to $f(t \to \infty, \tau) = 1$ over a characteristic time τ. To assess the accuracy of the initialization protocol, we evaluate the overlap [78]

$$O\left(\hat{A}, \hat{B}\right) \equiv \frac{\text{Tr}(\hat{A}^\dagger \hat{B})}{\sqrt{\text{Tr}(\hat{A}^\dagger \hat{A}) \, \text{Tr}(\hat{B}^\dagger \hat{B})}} \qquad (26)$$

between the prepared state $\hat{\rho}(t)$ and the encoding state $|0_L\rangle\langle 0_L| + |1_L\rangle\langle 1_L|$. For very small values of η, this protocol leads to the desired state manifold but it is characterized by unwanted fast oscillations around the target state. These are due to the phase accumulation through the sweep and they hinder the exact initialization of the code. We verify that choosing $\Delta_0 \ll -G$, where the steady state is vacuumlike, leads to similar results, with the size of the oscillations around the ideal value increasing as the system approaches the critical value $\Delta_0 = -G$. In Fig. 9, we show that a slightly larger value of η, for the same choice of Δ_0, suppresses these unwanted oscillations, further increasing the fidelity of the produced state. Notably, this choice does not significantly displace Γ from its optimal value [cf., e.g., Fig. 2(b)]. This result further advocates in favor of a hybrid operation of the cat instead of the Kerr limit, even in photon-loss-dominated configurations.
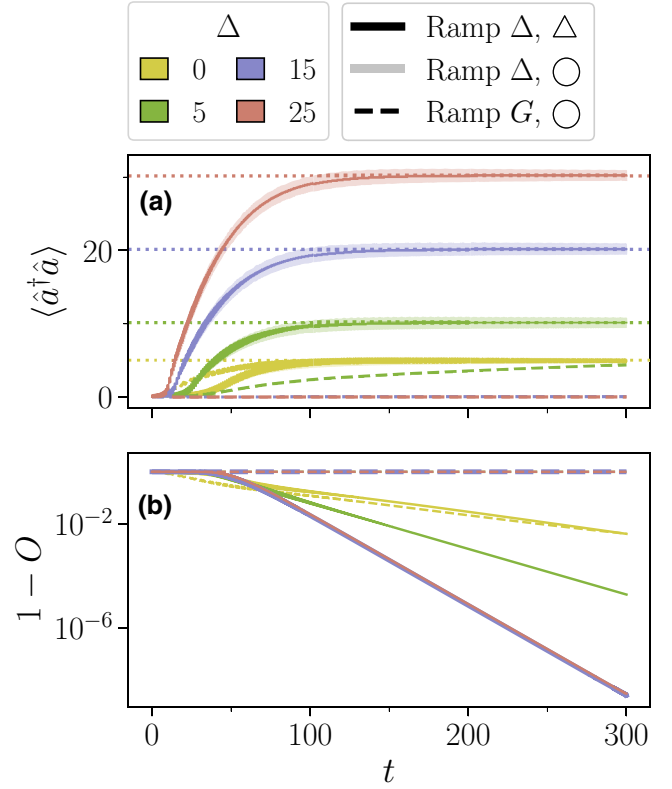

FIG. 9. The time-dependent simulation of the initialization protocols detailed in the text. The colors and symbols in the legend correspond to those points selected in the phase diagram of Fig. 8. The dashed lines represent the adiabatic ramping of $G(t) = f(t, \tau) G$, where $f(t, \tau) = \tanh(t/\tau)$, with $\tau = 50$ and $G = 5$. The solid lines describe $\Delta(t) = \Delta_0 + f(t, \tau)(\Delta - \Delta_0)$ for $\Delta_0 = -10$ and $U/\eta = 5 \times 10^2$. The shaded lines describe the amplitude of the oscillation for the same $\Delta(t)$ protocol, setting $U/\eta = 10^5$. (a) The evolution of the photon number during the initialization protocol. The dotted horizontal lines define the desired photon number for the different detuning configurations. (b) The quantity $1 - O$ as defined in Eq. (26), describing the similarity between the prepared state and the encoding one. We consider $\kappa_1 = 10^{-3} \gg 10^{-5} = \kappa_\phi$.

V. RESISTANCE TO FREQUENCY SHIFTS

As discussed in Ref. [33,34], random shifts in the resonant frequency of the oscillator can significantly hinder the performance of the code. In most cases, these effects can be modeled by an additional correlated noise in the form of an effective detuning $\Delta_{\text{err}}\hat{a}^\dagger\hat{a}$ acting on the system for a limited time t_0, representing, e.g., the typical time of gate operations. Common sources of shifts are cross-Kerr interactions originating either from spurious interactions with dissipatively coupled qubits or from stochastic jumps and thermal excitations in reservoir modes nonlinearly coupled to the system by, e.g., Josephson junctions. Because quantum information can be efficiently encoded over the whole

broken-symmetry region as in that realizing the metastable encoding, we anticipate the effect of such shifts to be far less detrimental for the critical cat code.

To demonstrate this claim, we consider the following protocol. The system is initialized in the state $\hat{\rho}(0) = |0_L\rangle\langle 0_L|$ and subsequently quenched with an additional detuning Δ_{err}. The system evolves under $\mathcal{L}'\hat{\rho} = \mathcal{L}_0\hat{\rho} - i\Delta_{\text{err}}[\hat{a}^\dagger\hat{a}, \hat{\rho}]$ for a time $t_0 = 10$ at which point Δ_{err} is switched off, leaving the system to stationarize under $\mathcal{L}_0$ over a time $t_1 = 5$.

Figure 10 shows the orthogonality $1 - O$ as a function of Δ and U/η. O is the overlap between the initial and the final states. It is defined by

$$O \equiv \text{Tr}\left[\hat{\rho}(0)\,\hat{\rho}(t_0 + t_1)\right] = \text{Tr}\left[\hat{\rho}(0)\,e^{\mathcal{L}_0 t_1}e^{\mathcal{L}' t_0}\hat{\rho}(0)\right]$$

$$(27)$$

and can be related to the evolution of the observables characterizing the system via the asymptotic projection method [33]. Figure 10(a) is computed for $\Delta_{\text{err}} = 1$. We choose this value in accordance with the discussion in Ref. [34, Appendix B3], specializing its result to the case of two coupled oscillators. The physical parameters characterizing the storage and reservoir modes are chosen by interpolating between those found in Refs. [18,19,29,31]. The data clearly identify a range of parameters in which the quantum information encoded in the critical cat is highly resilient to random frequency shifts. This region is characterized by positive values of Δ and $1 \lesssim U/\eta \lesssim 10^3$. A similar analysis for $\Delta_{\text{err}} = 4$ is shown in Fig. 10(b). This shows that even for very large frequency shifts, the critical cat still offers room for optimal encoding. This analysis further demonstrates the advantage of a hybrid encoding. We note, however, that the parameters granting optimal protection from frequency shifts do not coincide with those minimizing Γ. Nonetheless, a trade-off between these two optimal conditions can be found, although we anticipate the necessity for a complete characterization of these effects in coupled cat qubits when designing two-qubit gates or concatenation protocols, as also discussed in Ref. [34].

VI. BIAS-PRESERVING GATES

To harness the full potential of biased-noise qubits and retain their benefits throughout the computation, the gate operations must preserve the exponential suppression of bit-flip errors. Possible implementations of these *bias-preserving gates* rely on Zeno dynamics and topological deformation of the code space and have been extensively investigated in the resonant-dissipative and resonant-Hamiltonian configurations [9,25,28,34,42,43]. The very same protocols can be applied in the presence of nonvanishing detuning and in the hybrid-regime. This possibility has been extensively investigated in Refs. [25,30],
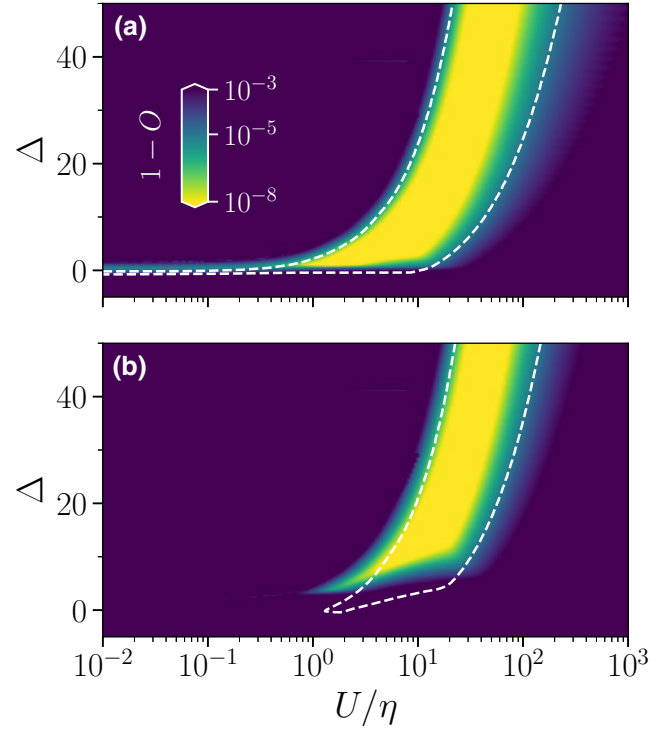

FIG. 10. The quantity $1 - O$, defined in Eq. (27), displayed as a function of the detuning Δ and of the angle θ in Eq. (20) for $\kappa_1 = 10^{-3} \gg \kappa_\phi = 10^{-5}$. The data are obtained by appropriately selecting at each point the correct encoding, either steady-state or metastable. The initial state $|0_L\rangle\langle 0_L|$ and the final state obtained from the recovery procedure are detailed in the text. The data in the two panels are computed assuming a frequency shift of (a) $\Delta_{\text{err}} = 1$ and (b) $\Delta_{\text{err}} = 4$. The white dashed lines bound the region wherein $1 - O < 10^{-5}$ in the cases (a) $\Delta_{\text{err}} = -1$ and (b) $\Delta_{\text{err}} = -4$.

also in relation to colored dissipation and superadiabatic pulse designs. To complete our investigation, we provide evidence of analogous benefits stemming from operating the qubit in the hybrid-detuned regime. We do so by investigating the simple example of the bias-preserving realization of a single qubit Z gate via $\hat{H}_Z = f(\hat{a} + \hat{a}^\dagger)$, where F is a weak drive. Indeed, $|+_L\rangle\langle+_L|$ and $|-_L\rangle\langle-_L|$ are states of opposite parity which can be connected by acting with $\hat{H}_Z$ for a time $T = \pi/(4F\text{Re}\{\alpha\})$. This is determined analytically by neglecting the effect of errors, setting $\Delta = 0$, and evaluating the action of $\hat{H}_Z$ on the manifold spanned by the pure cat states $|\mathcal{C}_\alpha^\pm\rangle$ with $\alpha = \sqrt{G/W}$. In the detuned regime, we find a similar expression for T with $\alpha = \sqrt{\langle\hat{a}^2\rangle}$. The optimal driving strength F maximizing the performance of the gate is determined by the competition between the adiabatic and nonadiabatic errors induced by the gate operation [20,27]. The adiabatic errors are those caused by the single-photon loss and dephasing events occurring during the action of the gate. The nonadiabatic errors, on the other hand, stem from diffusion out

of the code manifold induced by the driving field. Under these conditions, a trade-off must be found between these two sources of error.

Figure 11 provides a quantitative comparison of the performance of a Z gate in the hybrid-detuned, resonant-Hamiltonian, and resonant-dissipative configurations. Defining the error rates involves assessing the fidelity between the theoretically expected states and those obtained by time evolving under the action of gates. In agreement with the overarching literature [20,25,30], the total Z error is estimated by initializing the system in $|+_L\rangle\langle+_L|$ and evolving under $\mathcal{L}_Z\hat{\rho} = \mathcal{L}\hat{\rho} - i[\hat{H}_Z, \hat{\rho}]$ for a time T. The error probability P_Z is then defined as

$$P_Z = \frac{\left\langle\hat{\Pi}(T)\right\rangle + 1}{2}, \qquad (28)$$

exploiting the fact that after half a Rabi oscillation, the state of the system is expected to coincide with $|-_L\rangle\langle-_L|$, and that $\text{Tr}[\hat{\Pi}\,|\pm_L\rangle\langle\pm_L|] = \pm 1$, where we recall that $\hat{\Pi}$ is the parity operator. To evaluate P_X, we initialize the system in $|0_L\rangle\langle0_L|$, evolve under $\mathcal{L}_Z$ for a time T, and define

$$P_X = 1 - \left\langle\hat{S}(T)\right\rangle. \qquad (29)$$

The operator $\hat{S}$ quantifies whether the state is located in the right or left half plane of the phase space with respect to the line $\alpha \to -\alpha$ and is defined as

$$\hat{S} \equiv \text{sgn}\left(\cos(\phi)\hat{Q} + \sin(\phi)\hat{P}\right), \qquad (30)$$

where $\alpha = e^{i\phi}|\alpha|$, $\hat{Q} = (\hat{a} + \hat{a}^\dagger)/\sqrt{2}$, and $\hat{P} = -i(\hat{a} - \hat{a}^\dagger)/\sqrt{2}$.

Having obtained P_Z and P_X, we verify the bias preservation of the Z gate, expressed through the noise bias $\chi = P_Z/P_X$ in Fig. 11(c).

Our results confirm the viability of performing high-fidelity gates in the hybrid-detuned configuration and show a substantial improvement in the speed of gate operation in the critical regime with minimal impact on its fidelity, as well as a largely improved noise bias. In realistic computation, however, one needs also to asses how the gate performs when acting on an initial state deformed by the spurious processes of prior operations. In this paper, we consider the minimal example of the Z gate being applied after an idling time of the same duration of the Z gate itself, i.e., T. The results, displayed as dashed lines in Fig. 11(a), clearly demonstrate the advantage of the critical encoding over both the dissipative and Hamiltonian ones. Figures 11(b) and 11(c) demonstrate the noise bias being preserved under the action of consecutive operations.
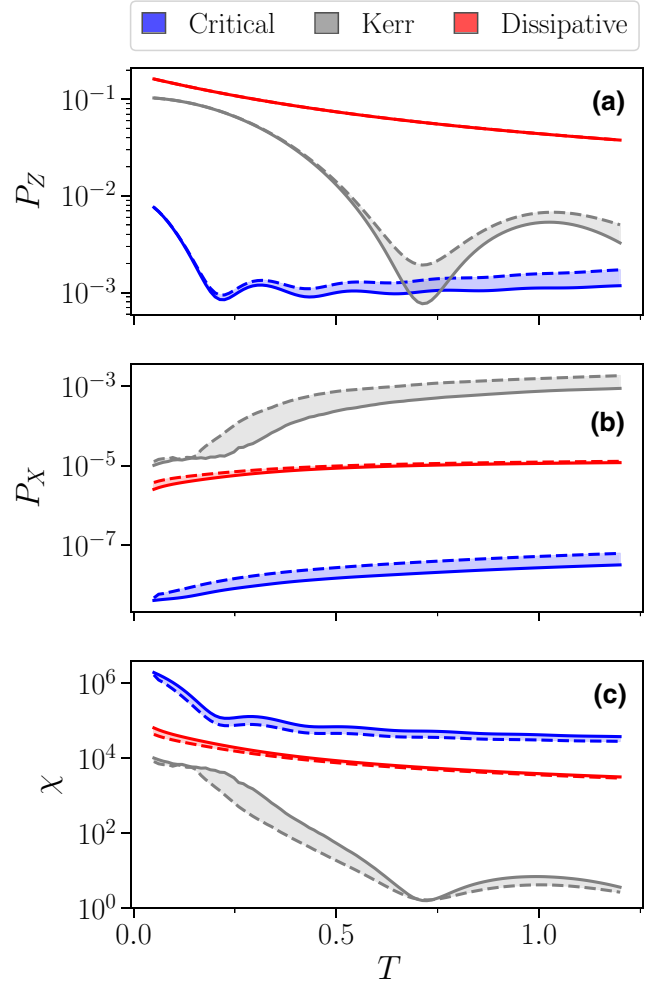

FIG. 11.   (a),(b) The total Z and X error probabilities of the Z gate as defined by Eqs. (28) and (29). (c) Their ratio, the noise bias $\chi = P_Z/P_X$. We consider three different operation regimes: critical ($\Delta = 40$, $U/\eta = 400$), Kerr ($\Delta = 0$, $U/\eta = \infty$), and dissipative ($\Delta = 0$, $U/\eta = 0$). The solid and dashed lines correspond to applying the gate at $t = 0$ or after an idling time of $t = T$, respectively. We consider the noise configuration $\kappa_1 = 10^{-5} \ll \kappa_\phi = 10^{-3}$.

VII. DISCUSSION AND CONCLUSIONS

We investigate the properties of the Schrödinger-cat code in the whole range of regimes between the two limiting cases of dissipative [9,18,19] and Kerr [26–29] cat code. We demonstrate that operating the cat code at finite values of the detuning between the two-photon driving field and the cavity frequency dramatically increases the resilience of the cat qubit to bit-flip errors. This improvement may require us to encode the information in the metastable manifold emerging from the first-order dissipative phase transition characterizing the driven-dissipative Kerr resonator at finite detuning [55]. We also discuss

how one needs to take into account several factors when discussing the performance of detuned cat codes. Beyond the phase-flip errors Γ, one has to explicitly take into account the fact that the system is metastable in many configurations and therefore a new error process, characterized by a rate Γ_{leak}, needs to be considered when discussing the quality of the encoding.

Our analysis of the bit-flip rate demonstrates that a small amount of two-photon loss already produces a significant improvement of the code performance with respect to the Kerr limit. Furthermore, we propose an efficient initialization protocol relying on small two-photon loss that circumvents the problems posed by the hysteresis of the vacuum and the metastable nature of the encoding. Two-photon loss is also beneficial for correcting frequency-shift errors that are expected to emerge in connected and concatenated cat architectures, as detailed in Ref. [34]. Finally, we show that bias-preserving gates perform significantly better in the hybrid-detuned case than in the Kerr and dissipative limits.

The picture emerging from our analysis is that focusing on a single a figure of merit to choose the optimal regime operation is reductive. All quantities considered here, namely Γ, Γ_{leak}, the resistance to frequency shifts, code initialization, and gate fidelity, advocate for a small, but non-negligible, two-photon loss rate being necessary for the optimal performance of the code. However, these quantities do not identify a unique global optimum. The optimal choice for the two-photon loss rate will ultimately depend on the specific of the platform under consideration.

All in all, dissipation and detuning emerge as pivotal and necessary resources for optimally efficient and reliable bosonic quantum encoding. From a broader perspective, our work demonstrates the nontrivial nature of dissipative processes in the presence of criticality. It suggests that the largely unexplored parameter space of all bosonic codes may still offer regions where specific properties of the code are enhanced, leading to a competitively efficient design of bosonic quantum code architectures.

ACKNOWLEDGMENTS

APPENDIX A: BOSONIC QUANTUM INFORMATION ENCODING

In this appendix, we focus on demonstrating the validity of the encoding for the different configurations explored in the main text. To do so, we first need to assess under which conditions a set of density matrices can encode quantum information and allow for quantum computation. Consider the six generic matrices $\hat{\rho}_{\pm X}$, $\hat{\rho}_{\pm Y}$, and $\hat{\rho}_{\pm Z}$. The first requirement for them to define a logical Bloch sphere is that the states on the opposite sides of the Bloch sphere are pairwise orthogonal. Having verified this, for them to support gate operations, one must also ensure that the structure they generate is isomorphic to

$$\hat{\rho} = \hat{Q} \otimes \hat{M}, \tag{A1}$$

where

$$
\begin{aligned}
\hat{Q} = &\, Q_{00} \, |0_L\rangle\langle 0_L| + Q_{11} \, |1_L\rangle\langle 1_L| \\
&\, + Q_{01} \, |0_L\rangle\langle 1_L| + Q_{10} \, |1_L\rangle\langle 0_L|
\end{aligned}
\tag{A2}
$$

is a 2×2 matrix defining the logical qubit and $\hat{M}$ a generic, possibly mixed, density matrix of a noisy system. If these conditions are satisfied, we can identify

$$
\begin{aligned}
\hat{\rho}_{\pm X} &\equiv \frac{|0_L\rangle\langle 0_L| + |1_L\rangle\langle 1_L| \pm |0_L\rangle\langle 1_L| \mp |1_L\rangle\langle 0_L|}{2} \otimes \hat{M}, \\
\hat{\rho}_{\pm Y} &\equiv \frac{|0_L\rangle\langle 0_L| + |1_L\rangle\langle 1_L| \mp i\,|0_L\rangle\langle 1_L| \pm i\,|1_L\rangle\langle 0_L|}{2} \otimes \hat{M}, \\
\hat{\rho}_{+Z} &\equiv |0_L\rangle\langle 0_L| \otimes \hat{M}, \quad \hat{\rho}_{-Z} \equiv |1_L\rangle\langle 1_L| \otimes \hat{M}.
\end{aligned}
\tag{A3}
$$

Operationally, to verify the validity of an encoding, we proceed as follows. Having identified possible candidates for $\hat{\rho}_{\pm X}$, $\hat{\rho}_{\pm Y}$, and $\hat{\rho}_{\pm Z}$, we verify the existence of a unitary transformation connecting them. To do so, we diagonalize $\hat{\rho}_{+Z}$ and $\hat{\rho}_{-Z}$, which, being orthogonal, commute and thus admit a common basis. By checking that their eigenvalues coincide, we verify that the matrix $\hat{M}$ associated with these states is the same. We then implement the permutation required for Eq. (A3) to be satisfied and call the combination of diagonalization and permutation of the two matrices, respectively, $\hat{R}_{+Z}$ and $\hat{R}_{-Z}$. Finally, we verify that Eq. (A3) is also satisfied by

$$
\begin{aligned}
\hat{R}_{+Z}\hat{R}_{-Z}\hat{\rho}_{\pm X}\hat{R}^{\dagger}_{-Z}\hat{R}^{\dagger}_{+Z}, \\
\hat{R}_{+Z}\hat{R}_{-Z}\hat{\rho}_{\pm Y}\hat{R}^{\dagger}_{-Z}\hat{R}^{\dagger}_{+Z},
\end{aligned}
\tag{A4}
$$

with the same $\hat{M}$.

Note that this construction only guarantees the possibility of encoding quantum information and performing gates at a single given time. The possibility of extending the validity of the encoding over time is tied to the action of the Liouvillian on span$\{\hat{\rho}_{\pm X}, \hat{\rho}_{\pm Y}, \hat{\rho}_{\pm Z}\}$. Indeed,

in the same way in which we have identified the isomorphism between the density matrices $\hat{\rho}_{\pm X}$, $\hat{\rho}_{\pm Y}$, $\hat{\rho}_{\pm Z}$ and the logical encoding, we can separate the action of the Liouvillian as

$$\mathcal{L} = \mathcal{L}_Q \oplus \mathcal{L}_M \oplus \mathcal{L}_{M \to Q} \oplus \mathcal{L}_{Q \to M}. \quad \text{(A5)}$$

While $\mathcal{L}_Q$ and $\mathcal{L}_M$ represent the action of the Liouvillian within $\hat{Q}$ and $\hat{M}$, $\mathcal{L}_{M \to Q}$ and $\mathcal{L}_{Q \to M}$ describe the processes connecting the logical manifold with the remainder of the Hilbert space containing $\hat{M}$. The different scenarios identified by Eqs. (16)–(19) correspond to the different ways in which $\mathcal{L}$ can act on the code space. Both the steady-state and metastable encodings discussed in Sec. IV can
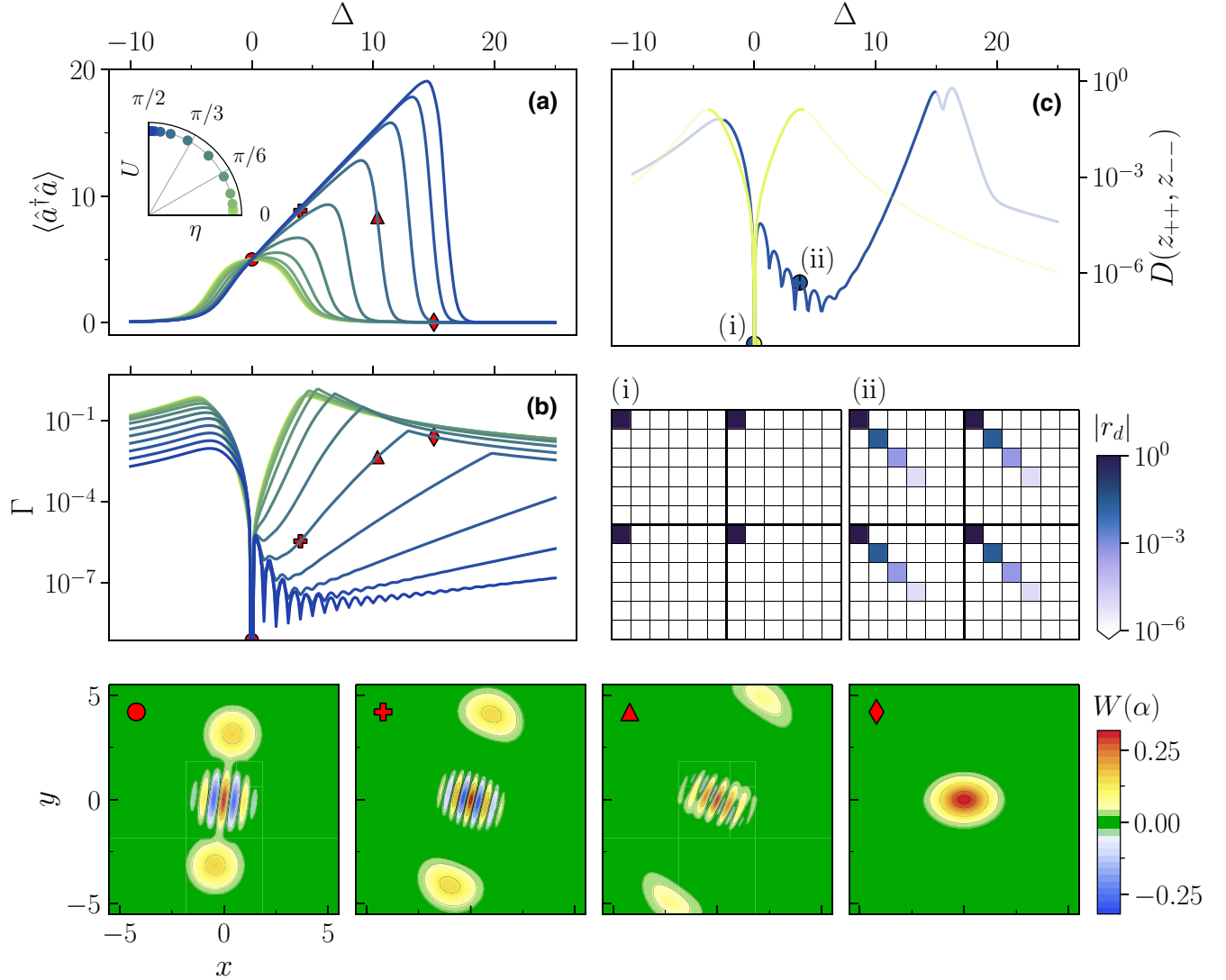

FIG. 12. The Liouvillian spectral analysis for $G = 5$ and different values of θ in Eq. (20). (a) The average occupation of the cavity as a function of the detuning Δ for different values of the Kerr nonlinearity U and two-photon loss η. As $|\alpha(\Delta = 0)|^2 = G/W$, all curves intersect at $\Delta = 0$. The jump in $\langle \hat{a}^\dagger \hat{a} \rangle$ appearing at $\Delta > 0$ becomes sharper for larger values of θ, heralding the emergence of a first-order phase transition. (b) The Liouvillian gap of the $+-$ symmetry sector $\Lambda_0^{+-} = \Gamma$. Optimal configurations with nonvanishing detuning appear as local minima of the curves and allow us to take advantage of the nonlinearity (see the text). In addition to this general trend, Γ exhibits dips for specific detuning values, namely, $\Delta = mU$ with $m \in \mathbb{N}$. These dips become more pronounced as the system approaches the Kerr limit, where they have recently been measured [32]. The insets to these plots display the Wigner distribution of $|1_L\rangle$ for $U/\eta = 5$ and increasing detuning values identified by red markers. (c) In an ideal noiseless subsystem, the eigenoperators $\hat{\rho}_0^{\mu\nu}$ obey $\hat{R}_\mu \rho_0^{\mu\nu} \hat{R}_\nu^\dagger \equiv |\mu\rangle\langle\nu| \otimes z_{\mu\nu}$, where $z_{\mu\nu} = z_{\mu'\nu'} \ \forall \mu, \nu, \mu', \nu'$ and $\hat{R}_\mu$ is the unitary transformation diagonalizing the density matrix $\hat{\rho}_0^{\mu\mu}$ [33]. We quantify the discrepancy from this ideal case using the trace distance between the two diagonal blocks z_{++} and z_{--}. We show this as a function of Δ for $2\theta/\pi = 0.01, 0.96$. The insets show the structure of the full density matrix for the points indicated in the main figure: (i) exemplifies a decoherence-free subspace and (ii) a noiseless subsystem with a mixed $\hat{M}$.

be seen as an extension of the ideas laid out for the ideal noiseless subsystem structure [13,23,52–54,79], which we briefly review below in relation to the driven-dissipative Kerr resonator.

1. Noiseless subsystem encoding

A noiseless subsystem is formally a subset of the Liouville space immune to the action of dissipation, making the logical information encoded therein transparent to any kind of error process. Indeed, the matrix $\hat{Q}$ in Eq. (A1) characterizing this encoding is stationary throughout the dynamics [cf. Eq. (17)]. This is always the case whenever $\hat{\rho}_{\pm X}$, $\hat{\rho}_{\pm Y}$, and $\hat{\rho}_{\pm Z}$ span the kernel of the Liouvillian. As detailed in Ref. [33], this requirement is equivalent to having four stationary processes: two steady states and two steady coherences. For the strongly $\mathcal{Z}_2$ symmetric Kerr resonator under investigation, this condition is only fulfilled for $\Delta = \kappa_1 = \kappa_\phi = 0$, that is, when the only dissipative process is two-photon loss.

Zero eigenvalues of the Liouvillian, however, are not only the hallmark of quantum information encoding but also one of the main signatures of DPTs. Indeed, the fourfold steady-state degeneracy necessary for an exact noiseless subsystem encoding can be achieved at $\Delta \neq 0$ through spontaneous breaking of the underlying symmetry of the model [33,71]. While this consideration is exact only in the thermodynamic limit of a DPT, precursors to these effects can be harnessed in *finite-size* systems. The question thus becomes: over which detuning region can an approximate noiseless subsystem encoding exist and

FIG. 14. A schematic representation of the states comprising the steady-state encoding defined in Eq. (A8).

to what extent does the introduction of a nonvanishing detuning destroy the encoding?

In a Liouvillian framework, the loss of quantum information introduced by the addition of a nonvanishing detuning is determined by the slowest relaxation rate of the off-diagonal Liouvillian sector, i.e., by $\Lambda_0^{+-} = \Lambda_0^{-+} = \Gamma$ [cf. Eq. (9)]. Indeed, while the strong $\mathcal{Z}_2$ symmetry
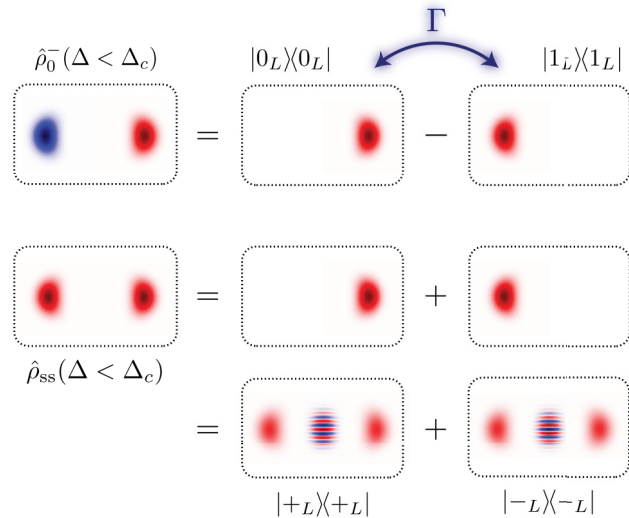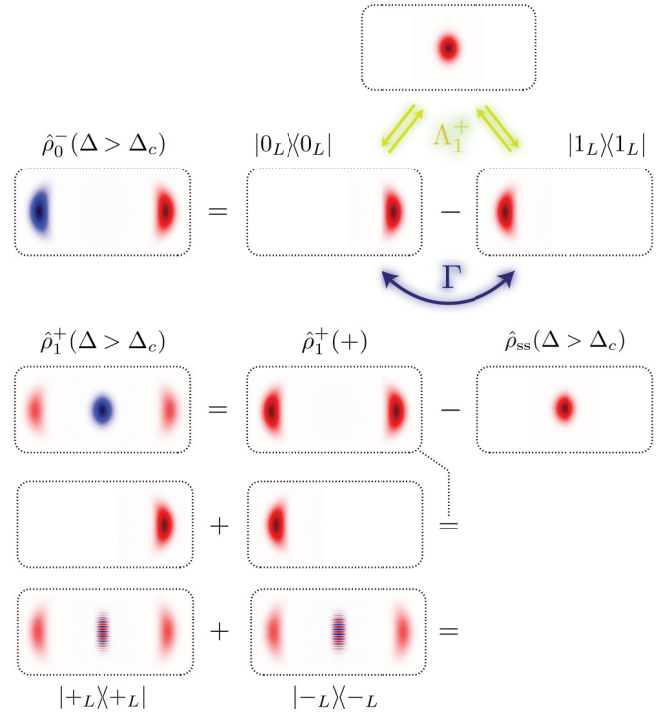

FIG. 13. A schematic representation of the states comprising the steady-state encoding defined in Eq. (A7). We show $\hat{\rho}_{\pm Z}$ and $\hat{\rho}_{\pm X}$. $\hat{\rho}_{\pm Y}$ can be obtained by acting on $\hat{\rho}_{\pm Z}$ with the rotation $\hat{X}_\varphi = \cos\frac{\varphi}{2}(\hat{\rho}_{+Z} + \hat{\rho}_{-Z}) + i\sin\frac{\varphi}{2}(\hat{\rho}_{+X} - \hat{\rho}_{-X})$ with $\varphi = \pi/2$.
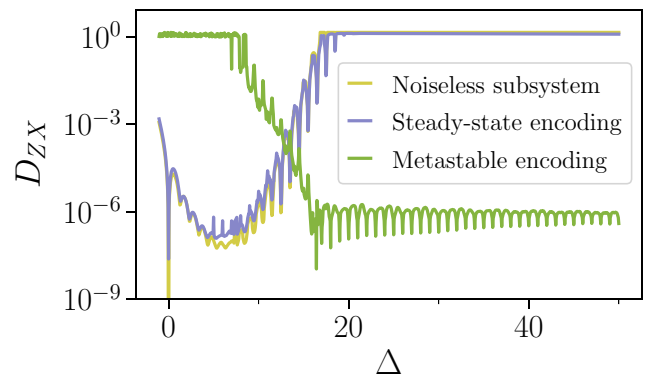

FIG. 15. The same distance quantifier as that used in Fig. 12(c). Here, it is evaluated between $\hat{\rho}_Z$ and $\hat{\rho}_X$, following the procedure detailed in the main text. We plot the results as a function of the detuning Δ for $\kappa_1 = 10^{-3} \gg \kappa_\phi = 10^{-5}$ and $G = 5$. The dips at integer values of detuning are to be imputed to the tunneling-suppression effects of Hamiltonian nature discussed in Ref. [32].
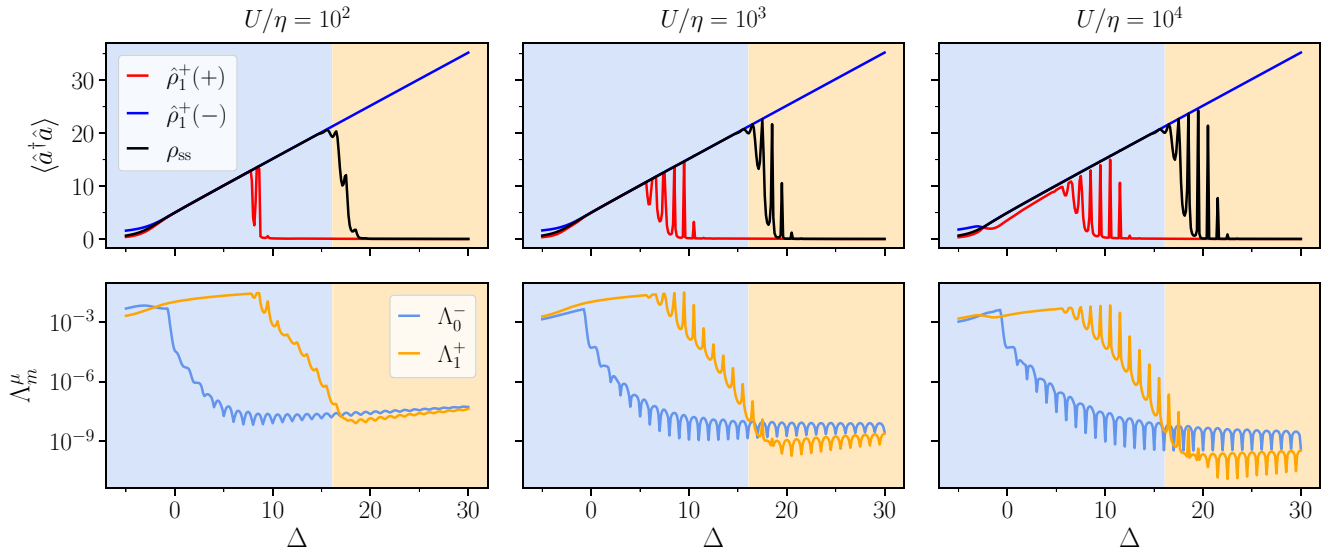
FIG. 16. The average photon number of the steady and metastable states as defined in the main text and the Liouvillian gaps Λ_1^+ and Λ_0^- as defined in Eq. (12) are shown as a function of the detuning Δ. The shaded blue (orange) area identifies the region hosting a steady-state (metastable) encoding. We consider $G = 5$ and $\kappa_1 = 10^{-3} \gg \kappa_\phi = 10^{-5}$.

ensures $\Lambda_0^{++} = \Lambda_0^{--} = 0$, the off-diagonal Liouvillian gap $\Lambda_0^{\pm,\mp}$ can still take finite values and should be minimized in order to suppress qubit decoherence. This quantity is shown in Fig. 12(b) and allows the identification of two regimes.

In the $U = 0$ case investigated in Ref. [33], the system displays *two* second-order phase transitions at $\Delta/G = \pm 1$, which symmetrically divide the phase space into a normal region ($|\Delta|/G > 1$), hosting at most a classical qubit structure, and a $\mathcal{Z}_2$-broken region ($|\Delta|/G < 1$),

where Λ_0^{+-} is small (zero in the TDL) and an approximate (exact in the TDL) noiseless subsystem structure emerges. For such vanishing nonlinearities, the broken-symmetry region is very narrow, the maximal photon number is attained at $\Delta = 0$, and it can be only increased by increasing G.

For finite U, the behavior of the system changes drastically, as the extent of the $\mathcal{Z}_2$-broken region wherein $\Lambda_0^{+-} \simeq 0$ increases far beyond the typical values obtained for $U \simeq 0$. Indeed, while the phase boundary for $\Delta <$
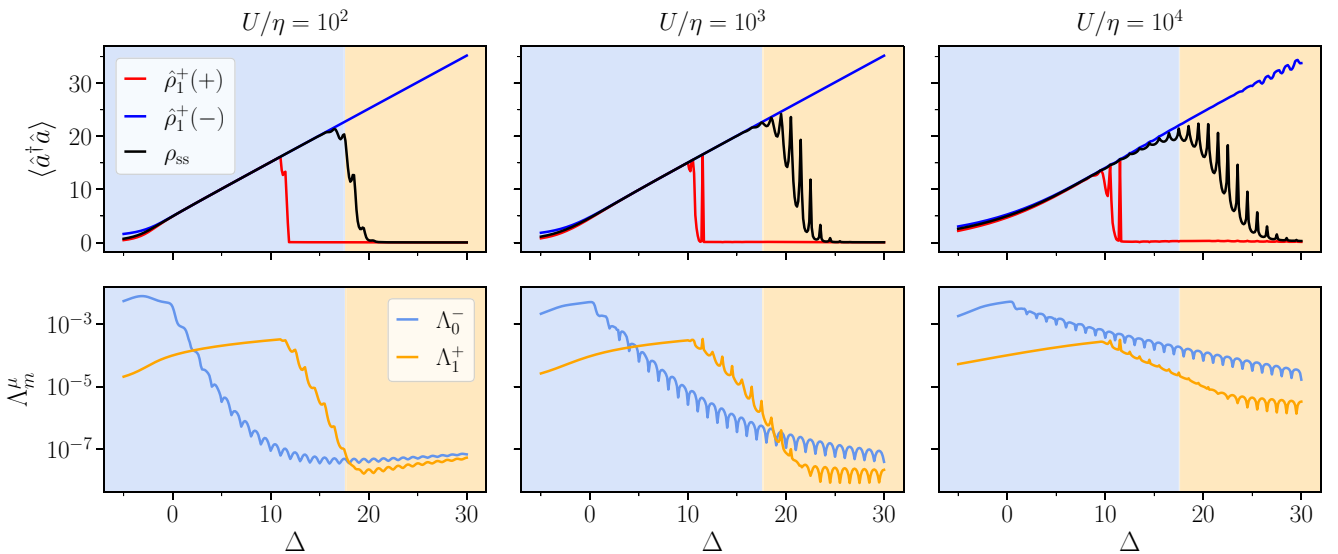

FIG. 17. The same as Fig. 16 but for $\kappa_1 = 10^{-5} \ll \kappa_\phi = 10^{-3}$.
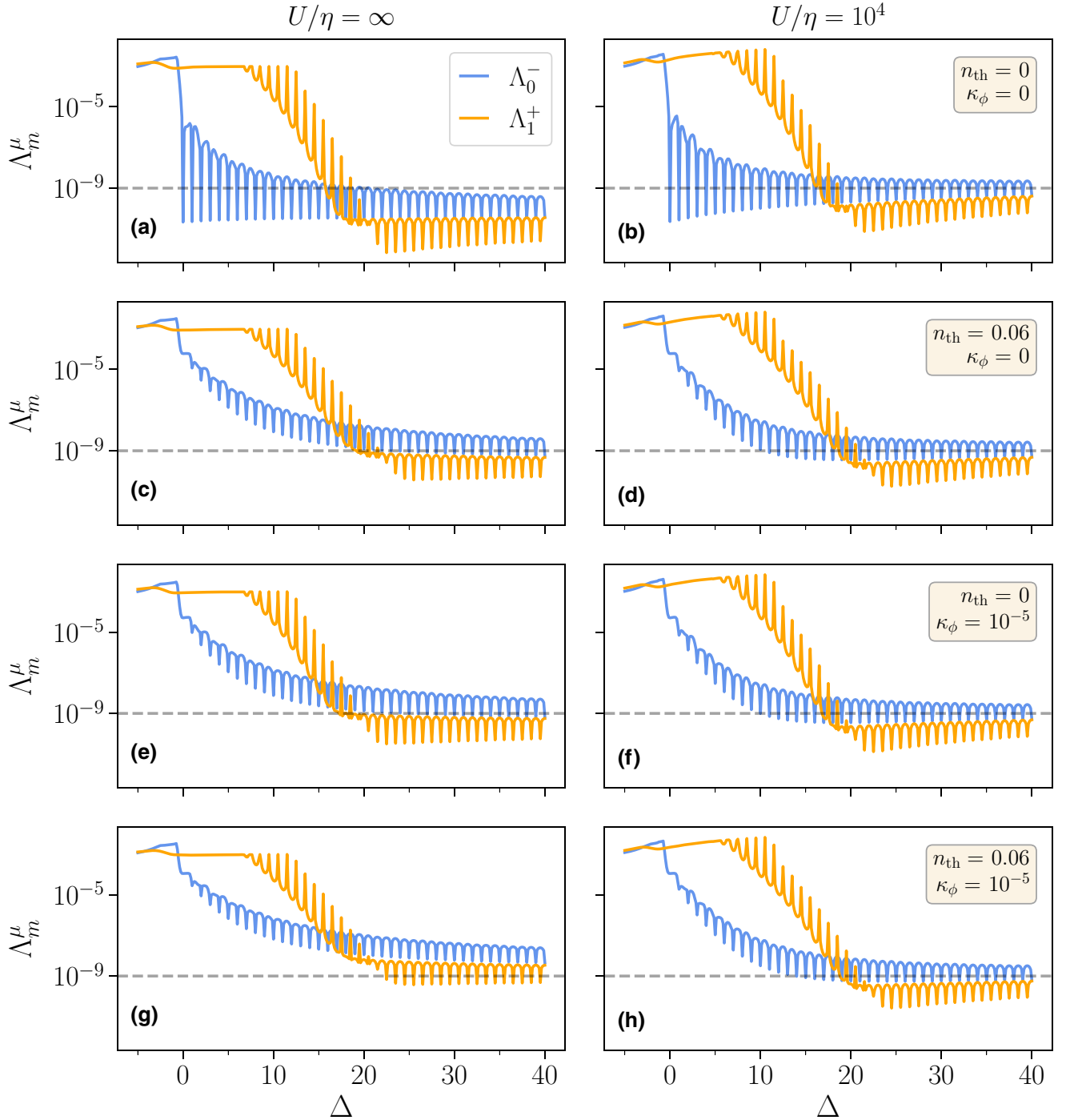
FIG. 18.   The Liouvillian gaps Λ_1^+ and Λ_0^- as defined in Eq. (12). The dephasing noise at rate κ_ϕ and the thermal excitations at rate $n_{\text{th}}\kappa_1$ are turned on separately, with the single-photon loss at rate $(1 + n_{\text{th}})\kappa_1$ underlying all of the simulations. The dashed line at $\Lambda = 10^{-9}$ serves as a guide to the eye to follow the considerations in the text. We set $\kappa_1 = 10^{-3}$, $n_{\text{th}} = 0.06$, and $\kappa_\phi = 10^{-5}$. Within the range of experimentally meaningful values of n_{th}, the one selected above allows us to immediately grasp the similar effects of dephasing and thermal noise.

0 is not significantly modified and the corresponding DPT is still of second order, for $\Delta > 0$, a *first-order* transition emerges at $\Delta/G \simeq \sqrt{1 + (U/\eta)^2}$ replacing the second-order one at $\Delta/G = 1$ for $U = 0$. This allows for

an approximately noiseless subsystem tensor structure to hold over a much broader region of positive detuning. In this regard, the use of a first-order DPT entails several advantages with respect to the proposal of Ref. [33].
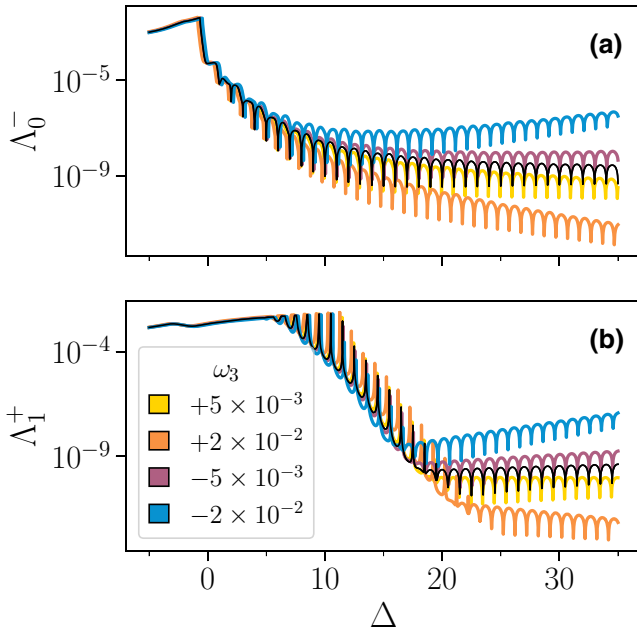
FIG. 19. The Liouvillian gaps (a) Λ_0^- and (b) Λ_1^+ as a function of the detuning Δ for different values of λ_3 in the perturbing Hamiltonian $\hat{H}_3$ defined in Eq. (B1). We set $U/\eta = 10^4$ and $\kappa_1 = 10^{-3} \gg \kappa_\phi = 10^{-5}$, with the black curve detailing the unperturbed behavior ($\lambda_3 = 0$).

Identifying the gradual transition from a second- to a first-order DPT are the elbowlike shape of the photon number for $U = 0$ in Fig. 12(a), which gradually evolves into a jump discontinuity for increasing values of U, and the precursors to a pointlike closure [71] of the diagonal gap Λ_1^{++} seen in Fig. 8(a).

Numerical evidence of the approximate fulfillment of Eq. (A3) is provided in Fig. 12(c). As explained above and in Ref. [33], we quantify the discrepancy from the ideal case via the trace distance

$$D(A, B) = \sqrt{\mathrm{Tr}\left[(A - B)^\dagger (A - B)\right]}$$

between the diagonal forms of $\hat{\rho}_{+Z}$ and $\hat{\rho}_{-Z}$. While in the dissipative limit $D(\hat{\rho}_{+Z}, \hat{\rho}_{-Z})$ only approaches zero in the vicinity of $\Delta = 0$, as the ratio of U/η is increased, small values of $D(\hat{\rho}_{+Z}, \hat{\rho}_{-Z})$ persist over a much wider range of positive detunings. Similar results are found for the distance from the orthogonal axes rotated according to Eq. (A4) (not shown). The insets below Fig. 12(c) are color plots of the absolute value of the matrix elements, for the two cases highlighted in the plot. They illustrate, respectively, a decoherence-free subspace steady state spanned by pure cat states and a noiseless subsystem steady state spanned by mixed states.

We conclude that a *steady* catlike state, capable of encoding quantum information, can be generated in the whole region $-G < \Delta < G\sqrt{1 + (U/\eta)^2}$. This state—the

Wigner representation of which is shown in the insets to Figs. 12(a) and 12(b) for increasing values of Δ—is not exactly the ideal cat described in Eq. (1), although it displays analogous properties.

2. Steady-state and metastable encoding

Having reviewed the ideal noiseless subsystem encoding, we generalize it to include biased-noise encoding and the possibility of encoding the system on metastable states.

The full Liouvillian $\mathcal{L}$ in Eq. (3) only possesses a weak $\mathcal{Z}_2$ symmetry, its steady state $\hat{\rho}_{ss} = \hat{\rho}_0^+$ is unique, and its generic density matrix decomposes along its eigenoperators as

$$\hat{\rho}(t) = \hat{\rho}_{ss} + \sum_{j \geq 0} c_j^-(t) \hat{\rho}_j^- + \sum_{j > 0} c_j^+(t) \hat{\rho}_j^+. \quad (A6)$$

Note that $\hat{\rho}_j^\mu$ are not physical density matrices, as they are in general neither positive nor have unit trace [80], and they acquire a physical meaning only through their eigendecomposition described in Eq. (21). Following the main text, we distinguish two regimes of operation wherein the nature of the encoding differs drastically.

Dropping the $\otimes \hat{M}$ notation for brevity, for $\Delta < \Delta_c$, the logical Z and X axes are identified by

$$\begin{aligned}
\hat{\rho}_0^- &= \hat{\rho}_0^-(+) - \hat{\rho}_0^-(-) \equiv |0_L\rangle\langle 0_L| - |1_L\rangle\langle 1_L| \\
\hat{\rho}_{ss} &= \hat{\rho}_{ss}(+) + \hat{\rho}_{ss}(-) = |+_L\rangle\langle +_L| + |-_L\rangle\langle -_L| \quad (A7) \\
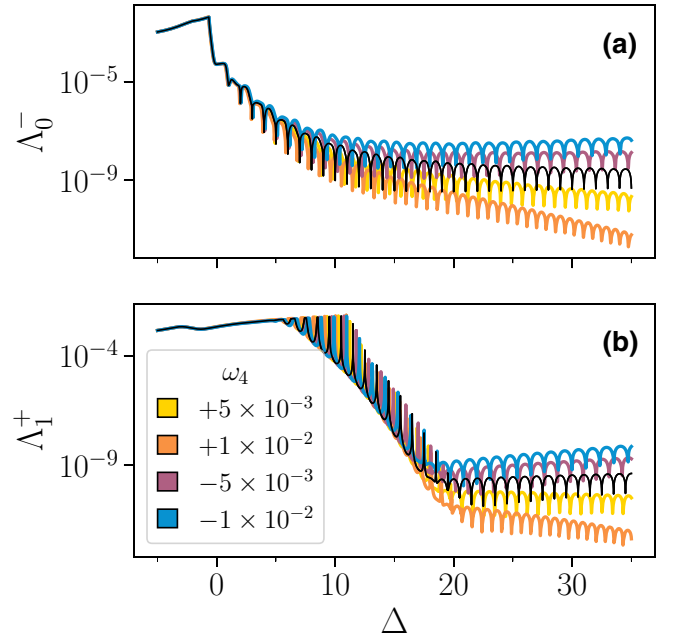&= |0_L\rangle\langle 0_L| + |1_L\rangle\langle 1_L|.
\end{aligned}$$

FIG. 20. The same as Fig. 19, with the Hamiltonian $\hat{H}_4$ defined in Eq. (B2) as the perturbing term.

In this regime, the unique steady state toward which the system decays coincides with the center of the logical Bloch sphere so that, although the matrix $\hat{Q}(t)$ evolves in time [cf. Eq. (18)], the dynamics are restricted to the code manifold. Specifically, the only process acting on the poles of the logical Bloch sphere is one that exchanges them at a rate $\Gamma = \Lambda_0^-$ (bit-flip error). The schematic representation of this encoding, which we deem to be *steady-state encoding*, is shown in Fig. 13.

For $\Delta > \Delta_c$, instead, the steady state approximately coincides with the vacuum and is no longer a viable choice for encoding the logical X axis. Nevertheless, the emergence of a second (almost) infinitely long-lived process $(\hat{\rho}_1^+)$ spanned by highly populated states still allows us to identify the logical Z and X axes as

$$\hat{\rho}_0^- = \hat{\rho}_0^-(+) - \hat{\rho}_0^-(-) \equiv |0_L\rangle\langle 0_L| - |1_L\rangle\langle 1_L|$$
$$\hat{\rho}_1^+(+) = \hat{\rho}_1^+(++) + \hat{\rho}_1^+(+-) = |+_L\rangle\langle +_L| + |-_L\rangle\langle -_L|.$$
$$(A8)$$

The rates at which these states decay can be obtained using the eigendecomposition in Eq. (A6). What we find is that, as depicted in Fig. 14, *only one* additional channel emerges that connects the poles of the Bloch sphere with the vacuum at a rate Λ_1^+, the dependence of which on Δ is characterized in Figs. 6 and 8. The metastable state $\rho_1^+(+)$ replaces the steady state as the center of the logical Bloch sphere, allowing us to extend the construction of steady-state encoding to incorporate metastability in what we dub a *metastable encoding*, whereby Eq. (19) follows.

Finally, in Fig. 15 we provide numerical evidence for the qubit structures defined in Eqs. (A7) and (A8) to satisfy Eq. (A1). Once again, we do so by evaluating the trace distance between the diagonal form of $\hat{\rho}_{\pm Z}$ and the matrix obtained by applying to $\hat{\rho}_{+X}$ the transformation in Eq. (A4). As Δ is increased, U/η is modified accordingly from point to point to ensure that $\Delta = \min[\Delta_{opt}(\theta), \Delta_{max}]$. We can clearly distinguish two regions: $\Delta < \Delta_c$, where the steady-state encoding approximates Eq. (A1) and the metastable one fails completely, and $\Delta > \Delta_c$, where the converse is true.

APPENDIX B: EXTENDED ANALYSIS OF Γ AND Γ_{leak}

We first extend the discussion on the relation between Γ and Γ_{leak} started in Sec. IV by repeating the same analysis presented in Figs. 6(a) and 6(b) for different choices of U/η and for both noise configurations. The results are shown in Figs. 16 and 17. We observe that the peaklike structure characterizing both Λ_0^- and Λ_1^+ discussed in the main text is gradually suppressed as η is increased. Moreover, as expected from Figs. 2(a) and 2(b), we note that the optimal detuning value minimizing Λ_0^- tends toward the steady-state encoding region (blue area) the higher is

the value of η (lower ratios U/η) that one considers. This encoding is not affected by any metastable time scale, thus voiding the trade-off between Λ_0^- and Λ_1^+ identified in the metastable encoding (orange area).

We further extend our analysis by taking into account the effects of thermal noise, as it has been identified as a leading source of error in Kerr-cat encodings [27,29]. In the Lindblad master equation [see Eq. (3)], its effect is captured by a term of the form $n_{th}\kappa_1 \mathcal{D}[\hat{a}^\dagger]$, where n_{th} is the equilibrium thermal-occupation number of the nonlinear resonator. In Fig. 18, we characterize the resilience of $\Gamma = \Lambda_0^-$ and $\Gamma_{leak} = \Lambda_1^+$ to such perturbations. To disentangle the thermal contributions from those of dephasing and single-photon loss, we activate the different noise channels separately, so that each of the four rows of Fig. 18 corresponds to a different noise configuration: Figs. 18(a) and 18(b) only single-photon loss, Figs. 18(c) and 18(d) single-photon loss and thermal noise, Figs. 18(e) and 18(f) single-photon loss and dephasing noise, and Figs. 18(g) and 18(h) single-photon loss and thermal and dephasing noise.

For these parameters, we compare the fully Hamiltonian limit ($U/\eta = \infty$) to a hybrid case ($U/\eta = 10^4$) allowing us to take advantage of criticality. From Figs. 18(a) and 18(b), we note that if $\kappa_\phi = n_{th} = 0$, all integer detuning values share the *same* value of Γ in the Hamiltonian limit, while the configuration with nonvanishing two-photon dissipation is optimal at resonance. This is no longer the case as soon as even the smallest amount of either dephasing or thermal noise is included. In this case, the value of Γ at low values of Δ rises substantially, leading to the considerations laid out in the main text.

In addition, comparison of Figs. 18(c) and 18(e) [and/or Figs. 18(d) and 18(f)] shows that dephasing and thermal noise affect Γ and Γ_{leak} in a similar way, allowing us to extend the conclusions drawn for dephasing in the main text to thermal noise as well.

Finally, Figs. 18(g) and 18(h) demonstrate the additional protection provided by a nonvanishing two-photon dissipation with respect to the combined effect of all the noise sources discussed above. This advocates once more in favor of operating in the critical regime.

The static effective Lindbladian in Eq. (3) is obtained from a low-order truncation of the perturbative expansion of a nonlinear microscopic Hamiltonian, e.g., the cosinusoidal potential of a Josephson junction [18]. To conclude, below we address the stability of our metastable solutions to the higher-order terms of this expansion. The leading resonant contributions that we take into account are the photon-number-dependent squeezing interaction

$$\hat{H}_3 = \lambda_3 (\hat{a}^\dagger \hat{a})(\hat{a}^{\dagger 2} + \hat{a}^2) \qquad (B1)$$

and the three-body interaction

$$\hat{H}_4 = \lambda_4 \hat{a}^{\dagger 3} \hat{a}^3. \tag{B2}$$

The analytical expressions for the coefficients of both terms are found in Ref. [31].

In Figs. 19 and 20, we detail the effect of $\hat{H}_3$ and $\hat{H}_4$ on Γ and Γ_{leak}, respectively. The changes in Γ and Γ_{leak} depend on both the magnitude and sign of the perturbations, with positive (negative) values of $\lambda_{j=3,4}$ favoring (hindering) the logical error rates. While these effects become more pronounced at larger detuning, the critical detuned regime remains the most advantageous one. It is finally worth noting that $\hat{H}_4$ introduces new minima in Γ and Γ_{leak}, while $\hat{H}_3$ simply shifts them. Analogous results are found in the Kerr limit ($U/\eta = \infty$) (not shown).

---

[1] D. A. Lidar and T. A. Brun, eds., *Quantum Error Correction* (Cambridge University Press, Cambridge, United Kingdom, 2013).

[2] S. Haroche and J.-M. Raimond, *Exploring the Quantum: Atoms, Cavities, and Photons* (Oxford University Press, Oxford, 2013).

[3] J. Preskill, Quantum computing in the NISQ era and beyond, Quantum **2**, 79 (2018).

[4] H.-P. Breuer and F. Petruccione, *The Theory of Open Quantum Systems* (Oxford University Press, Oxford, 2007).

[5] M. A. Nielsen and I. L. Chuang, *Quantum Computation and Quantum Information: 10th Anniversary Edition* (Cambridge University Press, New York, 2011), 10th ed.

[6] E. T. Campbell, B. M. Terhal, and C. Vuillot, Roads towards fault-tolerant universal quantum computation, Nature **549**, 172 (2017).

[7] B. M. Terhal, Quantum error correction for quantum memories, Rev. Mod. Phys. **87**, 307 (2015).

[8] D. Gottesman, A. Kitaev, and J. Preskill, Encoding a qubit in an oscillator, Phys. Rev. A **64**, 012310 (2001).

[9] M. Mirrahimi, Z. Leghtas, V. V. Albert, S. Touzard, R. J. Schoelkopf, L. Jiang, and M. H. Devoret, Dynamically protected cat-qubits: A new paradigm for universal quantum computation, New J. Phys. **16**, 045014 (2014).

[10] W. Cai, Y. Ma, W. Wang, C.-L. Zou, and L. Sun, Bosonic quantum error correction codes in superconducting quantum circuits, Fundam. Res. **1**, 50 (2021).

[11] A. Joshi, K. Noh, and Y. Y. Gao, Quantum information processing with bosonic qubits in circuit QED, Quantum Sci. Technol. **6**, 033001 (2021).

[12] B. M. Terhal, J. Conrad, and C. Vuillot, Towards scalable bosonic quantum error correction, Quantum Sci. Technol. **5**, 043001 (2020).

[13] E. Knill, R. Laflamme, and L. Viola, Theory of Quantum Error Correction for General Noise, Phys. Rev. Lett. **84**, 2525 (2000).

[14] M. H. Michael, M. Silveri, R. T. Brierley, V. V. Albert, J. Salmilehto, L. Jiang, and S. M. Girvin, New Class of Quantum Error-Correcting Codes for a Bosonic Mode, Phys. Rev. X **6**, 031006 (2016).

[15] D. S. Schlegel, F. Minganti, and V. Savona, Quantum error correction using squeezed Schrödinger cat states, arXiv:2201.02570 (2022).

[16] V. V. Albert, Lindbladians with multiple steady states: Theory and applications, arXiv:1802.00010 (2018).

[17] L. Gilles, B. M. Garraway, and P. L. Knight, Generation of nonclassical light by dissipative two-photon processes, Phys. Rev. A **49**, 2785 (1994).

[18] Z. Leghtas, S. Touzard, I. M. Pop, A. Kou, B. Vlastakis, A. Petrenko, K. M. Sliwa, A. Narla, S. Shankar, M. J. Hatridge, M. Reagor, L. Frunzio, R. J. Schoelkopf, M. Mirrahimi, and M. H. Devoret, Confining the state of light to a quantum manifold by engineered two-photon loss, Science **347**, 853 (2015).

[19] S. Touzard, A. Grimm, Z. Leghtas, S. O. Mundhada, P. Reinhold, C. Axline, M. Reagor, K. Chou, J. Blumoff, K. M. Sliwa, S. Shankar, L. Frunzio, R. J. Schoelkopf, M. Mirrahimi, and M. H. Devoret, Coherent Oscillations inside a Quantum Manifold Stabilized by Dissipation, Phys. Rev. X **8**, 021005 (2018).

[20] Q. Xu, J. K. Iverson, F. G. S. L. Brandão, and L. Jiang, Engineering fast bias-preserving gates on stabilized cat qubits, Phys. Rev. Res. **4**, 013082 (2022).

[21] H. Goto, Universal quantum computation with a nonlinear oscillator network, Phys. Rev. A **93**, 050301 (2016).

[22] P. T. Cochrane, G. J. Milburn, and W. J. Munro, Macroscopically distinct quantum-superposition states as a bosonic code for amplitude damping, Phys. Rev. A **59**, 2631 (1999).

[23] V. V. Albert, B. Bradlyn, M. Fraas, and L. Jiang, Geometry and Response of Lindbladians, Phys. Rev. X **6**, 041031 (2016).

[24] V. V. Albert, K. Noh, K. Duivenvoorden, D. J. Young, R. T. Brierley, P. Reinhold, C. Vuillot, L. Li, C. Shen, S. M. Girvin, B. M. Terhal, and L. Jiang, Performance and structure of single-mode bosonic codes, Phys. Rev. A **97**, 032346 (2018).

[25] R. Gautier, A. Sarlette, and M. Mirrahimi, Combined Dissipative and Hamiltonian Confinement of Cat Qubits, PRX Quantum **3**, 020339 (2022).

[26] S. Puri, S. Boutin, and A. Blais, Engineering the quantum states of light in a Kerr-nonlinear resonator by two-photon driving, npj Quantum Inf. **3**, 1 (2017).

[27] S. Puri, A. Grimm, P. Campagne-Ibarcq, A. Eickbusch, K. Noh, G. Roberts, L. Jiang, M. Mirrahimi, M. H. Devoret, and S. M. Girvin, Stabilized Cat in a Driven Nonlinear Cavity: A Fault-Tolerant Error Syndrome Detector, Phys. Rev. X **9**, 041009 (2019).

[28] S. Puri, L. St-Jean, J. A. Gross, A. Grimm, N. E. Frattini, P. S. Iyer, A. Krishna, S. Touzard, L. Jiang, A. Blais, S. T. Flammia, and S. M. Girvin, Bias-preserving gates with stabilized cat qubits, Sci. Adv. **6**, eaay5901 (2020).

[29] A. Grimm, N. E. Frattini, S. Puri, S. O. Mundhada, S. Touzard, M. Mirrahimi, S. M. Girvin, S. Shankar, and M. H. Devoret, Stabilization and operation of a Kerr-cat qubit, Nature **584**, 205 (2020).

[30] D. Ruiz, R. Gautier, J. Guillaud, and M. Mirrahimi, Two-photon driven Kerr quantum oscillator with multiple spectral degeneracies, arXiv:2211.03689 (2022).

[31] N. E. Frattini, R. G. Cortiñas, J. Venkatraman, X. Xiao, Q. Su, C. U. Lei, B. J. Chapman, V. R. Joshi, S. M. Girvin, R. J. Schoelkopf, S. Puri, and M. H. Devoret, The squeezed Kerr oscillator: Spectral kissing and phase-flip robustness, arXiv:2209.03934 (2022).

[32] J. Venkatraman, R. G. Cortinas, N. E. Frattini, X. Xiao, and M. H. Devoret, Quantum interference of tunneling paths under a double-well barrier, arXiv:2211.04605 (2022).

[33] S. Lieu, R. Belyansky, J. T. Young, R. Lundgren, V. V. Albert, and A. V. Gorshkov, Symmetry Breaking and Error Correction in Open Quantum Systems, Phys. Rev. Lett. **125**, 240405 (2020).

[34] C. Chamberland, K. Noh, P. Arrangoiz-Arriola, E. T. Campbell, C. T. Hann, J. Iverson, H. Putterman, T. C. Bohdanowicz, S. T. Flammia, A. Keller, G. Refael, J. Preskill, L. Jiang, A. H. Safavi-Naeini, O. Painter, and F. G. Brandão, Building a Fault-Tolerant Quantum Computer Using Concatenated Cat Codes, PRX Quantum **3**, 010329 (2022).

[35] C. Gerry and P. Knight, *Introductory Quantum Optics* (Cambridge University Press, Cambridge, United Kingdom, 2004).

[36] Note that this choice is arbitrary. An equivalently popular convention defines the logical basis as $|0_L\rangle = |\mathcal{C}_\alpha^+\rangle$, $|1_L\rangle = |\mathcal{C}_\alpha^-\rangle$. This amounts to a $\pi/2$ rotation within the logical space and an exchange between bit- and phase-flip errors.

[37] E. E. Hach III and C. C. Gerry, Generation of mixtures of Schrödinger-cat states from a competitive two-photon process, Phys. Rev. A **49**, 490 (1994).

[38] V. Gorini, A. Kossakowski, and E. C. G. Sudarshan, Completely positive dynamical semigroups of N-level systems, J. Math. Phys. **17**, 821 (1976).

[39] V. Gorini, A. Frigerio, M. Verri, A. Kossakowski, and E. C. G. Sudarshan, Properties of quantum Markovian master equations, Rep. Math. Phys. **13**, 149 (1978).

[40] G. Lindblad, On the generators of quantum dynamical semigroups, Commun. Math. Phys. **48**, 119 (1976).

[41] R. Lescanne, M. Villiers, T. Peronnin, A. Sarlette, M. Delbecq, B. Huard, T. Kontos, M. Mirrahimi, and Z. Leghtas, Exponential suppression of bit-flips in a qubit encoded in an oscillator, Nat. Phys. **16**, 509 (2020).

[42] J. Guillaud and M. Mirrahimi, Repetition Cat Qubits for Fault-Tolerant Quantum Computation, Phys. Rev. X **9**, 041053 (2019).

[43] J. Guillaud and M. Mirrahimi, Error rates and resource overheads of repetition cat qubits, Phys. Rev. A **103**, 042413 (2021).

[44] R. Blume-Kohout, H. K. Ng, D. Poulin, and L. Viola, Information-preserving structures: A general framework for quantum zero-error information, Phys. Rev. A **82**, 062306 (2010).

[45] B. Buča and T. Prosen, A note on symmetry reductions of the Lindblad equation: Transport in constrained open spin chains, New J. Phys. **14**, 073007 (2012).

[46] C. Sánchez Muñoz, A. Lara, J. Puebla, and F. Nori, Hybrid Systems for the Generation of Nonclassical Mechanical

[47] States via Quadratic Interactions, Phys. Rev. Lett. **121**, 123604 (2018).

[47] C. Sánchez Muñoz, B. Buča, J. Tindall, A. González-Tudela, D. Jaksch, and D. Porras, Symmetries and conservation laws in quantum trajectories: Dissipative freezing, Phys. Rev. A **100**, 042113 (2019).

[48] J. Thingna and D. Manzano, Degenerated Liouvillians and steady-state reduced density matrices, Chaos: Interdisc. J. Nonlinear Sci. **31**, 073114 (2021).

[49] Z. Zhang, J. Tindall, J. Mur-Petit, D. Jaksch, and B. Buča, Stationary state degeneracy of open quantum systems with non-Abelian symmetries, J. Phys. A: Math. Theor. **53**, 215304 (2020).

[50] V. V. Albert and L. Jiang, Symmetries and conserved quantities in Lindblad master equations, Phys. Rev. A **89**, 022118 (2014).

[51] B. Buča, J. Tindall, and D. Jaksch, Non-stationary coherent quantum many-body dynamics through dissipation, Nat. Commun. **10**, 1730 (2019).

[52] D. A. Lidar, in *Quantum Information and Computation for Chemistry* (Wiley, 2014), p. 295.

[53] J. Kempe, D. Bacon, D. A. Lidar, and K. B. Whaley, Theory of decoherence-free fault-tolerant universal quantum computation, Phys. Rev. A **63**, 042307 (2001).

[54] D. A. Lidar, I. L. Chuang, and K. B. Whaley, Decoherence-Free Subspaces for Quantum Computation, Phys. Rev. Lett. **81**, 2594 (1998).

[55] N. Bartolo, F. Minganti, W. Casteels, and C. Ciuti, Exact steady state of a Kerr resonator with one- and two-photon driving and dissipation: controllable Wigner-function multimodality and dissipative phase transitions, Phys. Rev. A **94**, 033841 (2016).

[56] W. Casteels, R. Fazio, and C. Ciuti, Critical dynamical properties of a first-order dissipative phase transition, Phys. Rev. A **95**, 012128 (2017).

[57] T. Fink, A. Schade, S. Höfling, C. Schneider, and A. Imamoglu, Signatures of a dissipative phase transition in photon correlation measurements, Nat. Phys. **14**, 365 (2018).

[58] At finite driving strength, only the finite-size precursors of an actual phase transition are witnessed [60,67,71]. Here, the critical region encompasses a finite range of detunings where the system crosses over from the highly populated phase to the other, by showing a series of peaks in the photon number. We define Δ_c as the median value of this critical region.

[59] M. Aspelmeyer, T. J. Kippenberg, and F. Marquardt, Cavity optomechanics, Rev. Mod. Phys. **86**, 1391 (2014).

[60] A. Biella, F. Storme, J. Lebreuilly, D. Rossini, R. Fazio, I. Carusotto, and C. Ciuti, Phase diagram of incoherently driven strongly correlated photonic lattices, Phys. Rev. A **96**, 023839 (2017).

[61] H. J. Carmichael, Breakdown of Photon Blockade: A Dissipative Quantum Phase Transition in Zero Dimensions, Phys. Rev. X **5**, 031028 (2015).

[62] W. Casteels and C. Ciuti, Quantum entanglement in the spatial-symmetry-breaking phase transition of a driven-dissipative Bose-Hubbard dimer, Phys. Rev. A **95**, 013812 (2017).

[63] M. Fitzpatrick, N. M. Sundaresan, A. C. Y. Li, J. Koch, and A. A. Houck, Observation of a Dissipative Phase Transition in a One-Dimensional Circuit QED Lattice, Phys. Rev. X **7**, 011016 (2017).

[64] E. M. Kessler, G. Giedke, A. Imamoglu, S. F. Yelin, M. D. Lukin, and J. I. Cirac, Dissipative phase transition in a central spin system, Phys. Rev. A **86**, 012116 (2012).

[65] F. Minganti, I. I. Arkhipov, A. Miranowicz, and F. Nori, Liouvillian spectral collapse in the Scully-Lamb laser model, Phys. Rev. Res. **3**, 043197 (2021).

[66] V. R. Overbeck, M. F. Maghrebi, A. V. Gorshkov, and H. Weimer, Multicritical behavior in dissipative Ising models, Phys. Rev. A **95**, 042133 (2017).

[67] R. Rota, F. Storme, N. Bartolo, R. Fazio, and C. Ciuti, Critical behavior of dissipative two-dimensional spin lattices, Phys. Rev. B **95**, 134431 (2017).

[68] R. Rota, F. Minganti, C. Ciuti, and V. Savona, Quantum Critical Regime in a Quadratically Driven Nonlinear Photonic Lattice, Phys. Rev. Lett. **122**, 110405 (2019).

[69] A. Rubio-García, R. Molina, and J. Dukelsky, From integrability to chaos in quantum Liouvillians, SciPost Physics Core **5**, 026 (2022).

[70] V. Savona, Spontaneous symmetry breaking in a quadratically driven nonlinear photonic lattice, Phys. Rev. A **96**, 033826 (2017).

[71] F. Minganti, Ph.D. thesis, Université Sorbonne Paris Cité, 2018.

[72] F. Vicentini, F. Minganti, R. Rota, G. Orso, and C. Ciuti, Critical slowing down in driven-dissipative Bose-Hubbard lattices, Phys. Rev. A **97**, 013853 (2018).

[73] A. Rivas and S. F. Huelga, *Open Quantum Systems: An Introduction*, Springer Briefs in Physics (Springer-Verlag, Berlin, 2012).

[74] F. Minganti, N. Bartolo, J. Lolli, W. Casteels, and C. Ciuti, Exact results for Schrödinger cats in driven-dissipative systems and their feedback control, Sci. Rep. **6**, 26987 (2016).

[75] R. Di Candia, F. Minganti, K. V. Petrovnin, G. S. Paraoanu, and S. Felicetti, Critical parametric quantum sensing, arXiv:2107.04503 (2021).

[76] T. Ilias, D. Yang, S. F. Huelga, and M. B. Plenio, Criticality-Enhanced Quantum Sensing via Continuous Measurement, PRX Quantum **3**, 010354 (2022).

[77] S. Fernández-Lorenzo and D. Porras, Quantum sensing close to a dissipative phase transition: Symmetry breaking and criticality as metrological resources, Phys. Rev. A **96**, 013817 (2017).

[78] We choose the overlap to quantify the resistance of the critical cat because it is more numerically stable than other indicators (e.g., the fidelity). Qualitatively analogous results are found using the fidelity.

[79] E. M. Fortunato, L. Viola, M. A. Pravia, E. Knill, R. Laflamme, T. F. Havel, and D. G. Cory, Exploring noiseless subsystems via nuclear magnetic resonance, Phys. Rev. A **67**, 062303 (2003).

[80] This is true for all $\hat{\rho}_j^\mu$ except for $\hat{\rho}_0^+ \equiv \hat{\rho}_{ss}$. To simplify the notation, we refer to $\hat{\rho}_j^\mu$ as any element in $\{\hat{\rho}_j^\mu\}_{\mu\in\{\pm\},j\in\mathbb{N}}/\{\hat{\rho}_0^+\}$ and use $\hat{\rho}_{ss}$ to identify $\hat{\rho}_0^+$.